Transient response to changes in uplift rates in the northern Atlas-Meseta system (Morocco)

The corrections made in this section will be reviewed and approved by a journal production editor.

R. Clementucci[a,b,*][Instruction: This is my email and should go below the affiliations. Thanks], rclementucci@ethz.ch, P. Ballato[a], L.L. Siame[b], C. Faccenna[a,c], S. Racano[d], G. Torreti[a], R. Lanari[e], L. Leanni[b], V. Guillou[b]

[a]Dipartimento di Scienze, Università Roma Tre, Largo San Leonardo Murialdo 1, 00146 Rome, Italy

[b]Aix-Marseille Univ., CNRS, IRD, INRAE, Collège de France, CEREGE, Aix-en Provence, France

[c]GFZ-German Research Centre for Geosciences, Potsdam, Germany

[d]Institute for Geosciences, University of Potsdam, Potsdam, Germany

[e]Dipartimento di Scienze, Università di Firenze, Italy

*Corresponding author at: Department of Earth Sciences, ETH Zurich, Zurich, Switzerland.

Abstract

Transient topography represents an opportunity for extracting information on the combined effect of tectonics, mantle-driven processes, lithology and climate across different temporal and spatial scales. The geomorphic signature of transient conditions can be used to unravel landscape evolution, especially in areas devoid of stratigraphic constraints. The topography of the Western Moroccan Meseta domain (WMM) is characterized by elevated non-lithological knickpoints, that delimit an uplifted relict landscape, implying a transient response to a change in uplift rate that occurred during the Cenozoic. Here, we determine denudation rates of selected watersheds and bedrock outcrops from cosmogenic nuclides and perform stream profile, regional and basin-scale geomorphic analysis. Denudation rates of the relict and the rejuvenated landscape range from 15 to 20 m/Myr and from 30 to 40 m/Myr, respectively. Rock uplift rates from river-profile inversions are 10–25 m/Myr from 45 to 22 Ma and 30–55 m/Myr from 22 to 10 Ma. Despite the different time scales, the inverted rates are consistent with ^{10}Be averaged denudation rates (15–20 and 30–40 m/Myr) and river incision values from Pleistocene lava flows (<10 and ~50 m/Myr) for the rejuvenated and relict regions of the WMM. These results agree with geological data and indicate that the observed ~400 m of surface uplift in the WMM started to develop possibly during the early Miocene (first phase). Given the wavelength of the topographic swell forming the topography of the WMM, uplift is here interpreted to reflect localized crustal thickening through magma addition or lithospheric thinning through mantle delamination. More recently, the occurrence of late Miocene marine sediments at ~1200 m of elevation indicates that the adjacent Folded Middle Atlas during the last 5–7 Ma experienced surface uplift at ~170–220 m/Myr. Considering the cumulative amount of surface uplift that varies eastward from 400 to 800 and 1200 m from the Meseta to the Tabular and the Folded Middle Atlas, as well as the spatio-temporal pattern of alkaline volcanism (middle Miocene and Pliocene to Present), we suggest that the most recent episode (second phase) of surface uplift was induced by a larger-scale process that most likely included upwelling of asthenospheric mantle and to a lesser extent crustal shortening in the Folded Middle Atlas.

Keywords:

Landscape evolution, Cosmogenic nuclides, Transient topography, Quantitative geomorphology, Atlas Mountains

Abbreviations

No keyword abbreviations are available

Data availability

No data was used for the research described in the article.

~~1.~~1 Introduction

The competition between crustal deformation, mantle driven uplift and surface processes modulates the growth and the decay of topography across diverse temporal and spatial scales (England and Molnar, 1990; Faccenna and Becker, 2020; Babault et al., 2022). Analytical solutions and numerical models suggest that topography should attain a steady state configuration when uplift is balanced by surface erosion (Whipple, 2001; Willett and Brandon, 2002). Conversely, when such a balance is not respected the landscape should be in disequilibrium conditions (*i.e.*, a transient landscape; *e.g.*, Olivetti et al., 2016; Godard et al., 2019; Clementucci et al., 2022, 2023). Transient landscapes represent the unique possibility to unravel the topographic evolution in areas devoid of stratigraphic constraints since the landscape still contains geomorphological features relative to the pre-perturbation stage. The transience results from different causes, such as base-level falls, drainage reorganizations, climate changes and/or variations in uplift rates at crustal and deeper scales (*e.g.*, Snyder et al., 2002; Roberts and White, 2010; Miller et al., 2013; Ballato et al., 2015; Sembroni et al., 2017; Gallen, 2018; Fernandes et al., 2019; Faccenna and Becker, 2020; Racano et al., 2021; Lanari et al., 2022). Therefore, the topography represents the superimposition of processes operating at multiple timescales and acting at different rates, wavelengths, and amplitudes. Although diverse approaches have been used to unpick these different signals, the combination of quantitative geomorphology with denudation data from cosmogenic nuclides and river profile inversion represents a powerful tool to infer the magnitude, timing, and rates of uplift through time (Miller et al., 2013; Goren et al., 2014; Pastor et al., 2015). This comprehensive approach allows for exploration of the uplift history of areas lacking stratigraphic constraints, with the potential to deconvolve the signals of topographic growth operating at different spatial scales. The surface expression of large-scale uplift and associated causes, in fact, remains often elusive mostly because the rates at which uplift occurs is poorly understood. Accordingly, the integrated approach outlined above can provide fundamental insights into geodynamic processes.

In this study, we focus on the Western Moroccan Meseta and the adjacent Tabular Middle Atlas, two tectonically quiescent domains of the Atlas-Meseta system (Fig. 1b). Despite quiescence, these relief features are characterized by elevated, extensive, low-gradient erosional surfaces bounded by steep hillslopes that are adjusting through fluvial incision, to a relative base level drop. This landscape is considered to represent a transient topography resulting from a Neogene phase of large-scale surface uplift, most likely driven by mantle upwelling (*i.e.*, topographic rejuvenation, *e.g.*, Missenard et al., 2006; Babault et al., 2008; Frizon de Lamotte et al., 2009; Miller and Becker,

2014; Clementucci et al., 2023; [Instruction: Lanari et al., 2023a]Lanari et al., 2023). The relict surfaces are characterized by a protracted phase of hillslope lowering, documented by low temperature thermochronology. Data suggests slow hillslope exhumation rates since the latest Cenozoic (<28 m/Ma if we consider a maximum cooling of 50 °C over the last 70 Ma and a geothermal gradient of 25 °C; see thermal modelling in Barbero et al., 2011 and also the recent review of Charton et al., 2021). These conditions provide a natural setting for investigating the mechanisms of large-scale uplift in tectonically inactive (or slow deforming) areas and quantifying rock uplift changes through time since the relict topography retains features of the pre-uplift event.

Images are optimised for fast web viewing. Click on the image to view the original version.

alt-text: Fig. 1

~~Fig. 1.~~Fig. 1

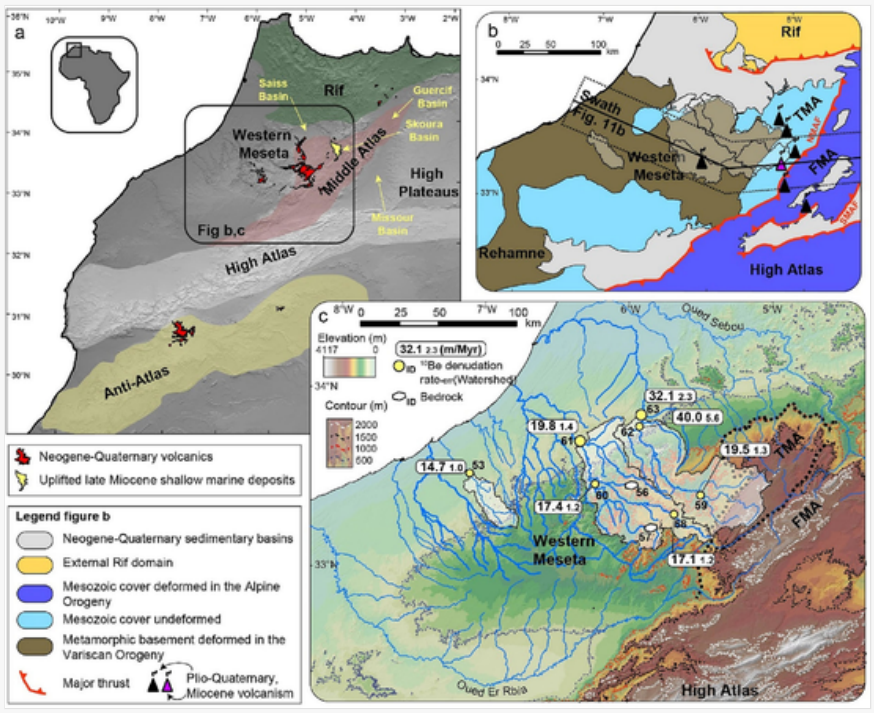

(a) Topographic hillshade of the Rif, Atlas and Meseta domains. (b) Morpho-structural domains in the western central Morocco and selected. FMA: Folded Middle Atlas. TMA: Tabular Middle Atlas. NMAF: North Middle Atlas fault. SMAF: South Middle Atlas fault. (c) DEM of the Western Moroccan Meseta. The white transparent areas show the sampled catchments while the dots show the location of the sampling points. Note the occurrence of two major catchment and several sub-catchments. The white hexagons show the location of bedrock samples. The thick dashed line indicates the boundary between the TMA, the FMA and the Western Meseta.

In this work, we combined denudation rates derived from *in situ*-produced cosmogenic nuclides (^{10}Be) with regional and basin-scale geomorphic analysis and river profile inversions. Specifically, we determined bedrock outcrops and basin-wide denudation rates from river-borne sediments to gauge them with basin-averaged geomorphic metrics (slope, local relief, and normalized steepness index). In addition, we estimated the magnitude of base-level fall by projecting the upper relict channels toward the present-day river mouth (*e.g.*, Miller et al., 2013; Sembroni et al., 2020). This allowed us to quantify the long-term magnitude of uplift of the Western Moroccan Meseta and the surrounding Tabular and Folded Middle Atlas domains. Moreover, we reconstructed the Cenozoic uplift history of the entire northern Atlas-Meseta system by combining the rock uplift evolution through time inferred from fluvial modelling with available geological data. Our results show consistent rates of denudation and rock uplift of the rejuvenated and the relict portions of the landscape through time and highlight the transient adjustment of hillslope and channels in response to a Cenozoic increase in rock uplift rates. Finally, we retraced back in time the uplift and the topographic evolution of the northern sector of the Atlas-Meseta orographic system and discussed possible driving mechanisms of the topographic rejuvenation.

~~2.~~2 Geological setting

The Atlas-Meseta of Morocco (NW Africa) includes mountain ranges (Anti-Atlas, High Atlas and Middle Atlas) elevated tabular areas (Western Meseta, Tabular Middle Atlas and High Plateaus), and sedimentary basins (Missour and Saiss among others; Fig. 1a). The WSW-ENE oriented, 4-km-high High Atlas represents the highest mountain range of the Atlas-Meseta system. It consists mainly of Mesozoic-Cenozoic syn- to post-rift deposits that were uplifted in the Eocene and Miocene (Arboleya et al., 2004; Lanari et al., 2020a). The central sectors of the High Atlas merge ~~towards~~toward the NE with the SW-NE-striking Middle Atlas (Fig. 1a). This range is formed by the same deposits of the High Atlas that were deformed most likely from the late Miocene, but with some angular unconformities suggesting a more complex Meso-Cenozoic history of deformation and sedimentation (Charriere, 1984). Topographically, the Middle Atlas can be divided into two morpho-structural domains known as the Tabular and Folded Middle Atlas (TMA and FMA; Fig. 1b), which are commonly interpreted as the flank (footwall) and the depocenter (hanging wall) of a Mesozoic rift, respectively (Gomez et al., 1996, 1998). The TMA domain ranges between 1500 and 2000 m of elevation and consists of Mesozoic limestones that are slightly tilted westward. The FMA reaches 3000 m of elevation and includes north-west- to south-east-verging folds mostly detached from the underlying basement along Triassic evaporites (Charriere, 1984; Gomez et al., 1998). The folded range is bounded to the northwest by the North Middle Atlas fault (NMAF) and to the southeast by the South Middle Atlas Fault (SMAF; Fig. 1b). The elevated Western Moroccan Meseta (WMM) and High Plateau (HP) rises to an elevation of 1500 m, without any evidence of Q6 Cenozoic tectonic deformation (Gomez et al., 1998~~9~~; Barbero et al., 2011). Particularly, the WMM is characterized by a complex assemblage of Paleozoic rocks deformed during the Variscan orogeny (Hoepffner et al., 2005; Fig. 1b). This includes Ordovician, Silurian, and Devonian schists and metasedimentary rocks, locally intruded by late Carboniferous granitoids (320 and 270 Ma; Hoepffner et al., 2005 and references therein). This domain is partially covered by undeformed Mesozoic and Eocene marine Q7 sedimentary rocks (*e.g.*, Phosphatic series; Salvan and Farkhany, 19~~54~~82; El Kiram et al., 2019; El Attmani et al., 2021). The Rif Mountains to the north reaches peaks of up to 2500 m and represents a fold and thrust belt that experienced NW-SE shortening due to the convergence of Africa and Eurasia (Jolivet and Faccenna, 2000; Abbassi et al., 2020; Agharroud et al., 2021). There, contractional deformation migrated southward until 8 Ma when the outermost tectonic units where emplaced onto the South Rifian Corridor (Krijgsman et al., 1999; Capella et al., 2018; Abbassi et al., 2020, 2022).

The High and Middle Atlas domains are characterized by strain partitioning with a total amount of shortening of ~24 %, accommodated by both thrust and oblique/strike-slip faults (Gomez et al., 1999; Lanari et al., 2020b). The amount of shortening across the thrust faults ranges between ~12 % and 15 % (Missenard et al., 2006; (Domènech et al., 2015); ~~Domenech et al., 2018;~~ [Instruction: 2023b]Lanari et al., 2020a, 2023) Q8 suggesting that crustal thickening is insufficient to isostatically support the modern topography (Arboleya et al., 2004; Missenard et al., 2006). Moreover, geophysical studies highlight the presence of an anomalously thin lithosphere beneath the entire Atlas-Meseta system (Miller and Becker, 2014; Miller et al., 2015). This is associated with continental intraplate volcanism that seems to be coeval with the main tectonic events (Missenard et al., 2006; El Azzouzi et al., 2010; Lanari et al., 2020a). The lavas are well exposed in the FMA, TMA, the WMM over a surface of about 960 km^2 and have a geochemical affinity with the Canary mantle plume composition ranging from basanite to alkali basalt (Duggen et al., 2009; El Azzouzi et al., 2010). The late Cenozoic phase of uplift is documented by the occurrence of late Miocene (Messinian) shallow-water marine deposits in the Skoura basin at ~1200 m of elevation (Babault et al., 2008) and the progressive shallowing upward trend of the Miocene marine sediments of the Saïss and Guercif basin (Fig. 1a; Krijgsman et al., 1999).

~~3.~~3 Methods

~~3.1.~~3.1 Topographic, stream analysis and long-term incision

A Shuttle Radar Topography Mission Digital Elevation Model (SRTM DEM, pixel size of 30 m) was used to extract the drainage network. Hillslope metrics, such as slope and local relief with a circular sampling window of 2.5 km radius, as well as channel and basin metrics were extracted using ArcGIS and the MATLAB software packages TopoToolbox (Schwanghart and Scherler, 2014) and Topographic Analysis Kit (TAK, Forte and Whipple, 2019), together with additional MATLAB functions (*e.g.*, [Instruction: this reference should be deleted]Gallen, 2018(Gallen and Wegmann, 2017)). The relationships between river channel steepness and erosion/uplift rates have been demonstrated in various geological settings (Kirby and Whipple, 2012). In detachment-limited conditions, these relationships are modulated by the stream-power model, which can be integrated, assuming spatially invariant uplift and erodibility, to estimate the integral quantity χ (details in the section S1; Perron and Royden, 2013). This allows transforming river longitudinal profiles to χ *versus* elevation (z) plots (here and thereafter defined as χ - z plot). Consequently, the slope in χ space is defined as the steepness index (k_s) when the reference area (A_0) is equal to 1. To compare k_s values of longitudinal profiles, a reference concavity index (θ_{ref}) of 0.45 is applied to derive the normalized channel steepness indices (k_{sn}; Kirby and Whipple, 2012 and references therein). The θ_{ref} was calculated by minimising the scatter in χ space of all rivers draining the study area (Perron and Royden, 2013; Goren et al., 2014; Fig. S1). Our θ_{ref} coincides with the value typically used to derive ~~normalised~~normalized channel steepness (Snyder et al., 2000; Kirby and Whipple, 2012).

Knickpoints were identified and discretized based on the shape of the streams in the longitudinal profiles and the χ - z plots and using available geological maps (Service Géologique du Maroc) and satellite imagery (Google Earth). Importantly, non-lithological knickpoints cluster around similar χ values and separate stream segments with different k_{sn} values (Perron and Royden, 2013; Clementucci, 2022). Using this approach, the knickpoints were divided into non-lithological, minor, lithological and man-made dam. Streams with knickpoints identified as transient (non-lithological) were used for reconstructing river projections to estimate the magnitude of long-term incision. Such profiles can be reconstructed using the k_{sn} values (θ_{ref} = 0.45) of the river segments upstream of the non-lithological knickpoints in the χ space, assuming that the paleo-river network remained approximately the same through time (Perron and Royden, 2013; Smith et al., 2022). Full details of equations and stream analysis are provided in the Supplementary material.

~~3.2.~~3.2 ^{10}Be-derived denudation rates

We measured the concentration of *in situ*-produced cosmogenic ^{10}Be in quartz from seven river-borne samples collected in active channels and from four bedrock outcrops (Fig. 1c; Table 1). The only lithologies exposed in the WMM that contain quartz are Paleozoic basement rocks such as schists, metasedimentary rocks, and granites. Our sampled catchments cover most of this area (Figs. 1b and S2), from the elevated relict to the steeper landscape portions. In one case we sampled a catchment with Paleozoic rocks at the periphery of the uplifted area (sample 53) to compare denudations rates from different sectors of the WMM (Fig. 1c). The basin-wide denudation rates were determined only from quartz-bearing rocks, which usually represent 50 to 100 % of the total area of the sampled catchments (Table S1). The portions of the sampled catchments with Mesozoic limestones were not considered in the scaling modelling (Clementucci et al., 2022 and references therein). Details of sample preparation, from the initial mineral separation to the final conversion of *in situ*-produced ^{10}Be to basin-wide denudation rates are provided in the Supplementary material S2. Catchments 58, 59, 60 and 62 are sub-catchments of two larger basins named 61 and 63, while catchment 53 corresponds to the westernmost sampling location (Fig. 1c). The upstream areas range between 30 and 100 km^2 and 320 and 350 km^2 for the sub-catchments and the larger basins, respectively. In particular, we selected samples 58 and 59 upstream of the low-relief surfaces and samples 61 and 63 downstream of the relict landscape to extract the denudation rates of the adjusted and steeper topography. Catchments 53, 58, 59, 62 and 63 are characterized by uniform quartz-bearing lithologies. Conversely, the contribution of quartz, in catchments 60 and 61, is mostly from two granite massifs exposed in the highest topography of the Moroccan Meseta region. To quantify the local denudation rates of the granite massifs forming the landscape of the western Meseta, we sampled four bedrock outcrops: two from the summit of an erosional surface (samples 56A, 56B) and two from sub-horizontal ridge crests located close to the margin of the relict topography (samples 57A, 57B, Table 1 and Fig. 1c).

alt-text: Table 1

~~Table 1.~~Table 1

The table layout displayed in this section is not how it will appear in the final version. The representation below is solely purposed for providing corrections to the table. To view the actual presentation of the table, please click on the Preview located at the top of the page.

Denudation rates from cosmogenic ^{10}Be in river borne sand and bedrock samples.

ID	Geomorphic position	Long.	Lat.	Elev.[a]	Quarz mass[b]	Carrier mass (^{9}Be)	10Be/9Be[c]		[^{10}Be][d] 10^3 (at./g)		Production rate[e] (at./g/yr)			Denudation (m/Myr)		Integration time[f] (yr)	
		°W	°N	(m)	(g)	(g)	Value (10^{-15})	Error (%)	Value	Error	Neutrons	Slow muons	Fast muons	Value	Error	Value	Error
53	Watershed	7.1500	33.5364	455	20.70	0.151	195.1	3.4	284.7	9.8	5.08	0.015	0.04	14.76	1.02	48,081	3330.1
58	Watershed	5.7512	33.2640	1173	21.82	0.150	292.6	4.3	406.0	17.6	8.69	0.02	0.05	17.11	1.27	41,624	3080.5
59	Watershed	5.5714	33.3807	1083	21.68	0.151	241.6	3.4	338.5	11.7	8.16	0.02	0.05	19.49	1.35	36,639	2535.6
60	Watershed	6.2790	33.4496	914	21.20	0.150	238.8	3.4	339.4	11.8	7.28	0.02	0.05	17.36	1.20	41,023	2845.5
62	Watershed	5.9743	33.7520	721	21.12	0.151	95.5	12.3	135.0	17.0	6.32	0.02	0.05	39.94	5.57	18,044	2514.7
Blank							0.45	51.3									
61	Watershed	6.365	33.698	928	21.47	0.152	211.5	3.3	302.7	10.3	7.35	0.02	0.05	19.80	1.37	36,076	2488.0
63	Watershed	5.931	33.829	1049	21.74	0.151	146.6	4.1	204.8	8.5	7.95	0.02	0.05	32.15	2.34	22,369	1630.0
56A	Summit	6.0535	33.4123	1124	21.84	0.150	1055.6	3.1	1467.4	46.0	8.43	0.02	0.05	3.46	0.23	163,446	11,064.1
56B	Summit	6.0535	33.4123	1124	21.59	0.150	900.1	2.5	1259.7	31.2	8.43	0.02	0.05	4.11	0.27	139,446	9053.0
57A	Ridge crest	5.8906	33.1922	1098	19.45	0.150	251.2	3.3	389.0	12.9	8.23	0.02	0.05	14.36	0.98	41,958	2874.7
57B	Ridge crest	5.8913	33.1919	1099	17.24	0.151	239.1	3.5	423.6	14.9	8.24	0.02	0.05	13.13	0.91	45,808	3185.9
Blank							0.788	23.05									

Table Footnotes

[a] Basin mean elevation.

[b] Mass of pure quartz dissolved.

[c] Isotopic ratio uncertainties include statistical error on counted ^{10}Be events (N) and analytical error correction.

[d] Uncertainties on ^{10}Be concentrations are calculated using the standard error propagation method using the quadratic sum of the relative errors associated to the counting statistics, AMS internal error (0.5 % for ASTER), and error associated to the process blank.

[e] Production rate is the spatially averaged production rate over the river basin, scaled for elevation, latitude (Stone, 2000) and geomorphic shielding (Dunne et al., 1999). The values, relative to watersheds, are calculated for a non-uniform distribution of quartz-lithologies in the sample basins (*e.g.*, Carretier et al., 2015; Clementucci et al., 2022).

[f] Integration times are calculated after Lal (1991) while their uncertainties are calculated propagating the error of the uncertainties associated with denudation rates.

In situ-produced ^{10}Be concentrations were converted to basin-wide denudation rates and bedrock erosion rates using the MATLAB scripts of Balco et al. (2008), which are based on the time-dependent scaling functions of Stone (2000)~~'~~s scheme that consider three different categories of particles responsible for the *in-situ* production of ^{10}Be (Braucher et al., 2011). The geomorphic shielding ((Dunne et al., 1999)Dunne et al., 1999), scaling factor of ~~Stone (2000)~~ (Stone, 2000) and the mean elevation of sampled catchments were determined for each pixel of the digital elevation model (DEM), considering only the areas contributing with quartz-bearing lithologies. In the scaling

model, λ describes the radioactive decay constant of ^{10}Be. Denudation rates from ^{10}Be concentrations were calculated using a ^{10}Be sea level high latitude production rate of 4.02 ± 0.33 atoms ^{10}Be (g-SiO_2)/yr (Borchers et al., 2016), and half-lives of (1.387 ± 0.012) × 10^6 years (Chmeleff et al., 2010; Korschinek et al., 2010). At cosmogenic steady-state, the cosmogenic ^{10}Be in river-borne quartz mineral records a time integrated spatially averaged denudation rate, which represents fluvially mixed denudation products of all the processes occurring in each watershed ((Granger et al., 1996)Granger et al., 1996). This integration occurs over the time needed to remove one attenuation length (*e.g.*, roughly 60 cm; Lal, 1991).

We also applied a sediment mixing correction to estimate a value of denudation for the downstream knickpoint portion of the catchment 63 (basin 64), knowing the denudation and drainage area of the whole catchment and the upper sub-catchment, upstream of the non-lithological knickpoints (Fig. 2; according to Granger et al., 1996; Miller et al., 2013; Rosenkranz et al., 2018):

$$D_{1\text{-}2} = \frac{D_1 A_1 - D_2 A_2}{A_1 - A_2} \quad (1)$$

where $A_1 - D_1$ and $A_2 - D_2$ are the drainage area and basin-wide denudation rate of the whole catchment and above the non-lithological knickpoint, respectively. $D_{1\text{-}2}$ is the basin-wide denudation of the adjusted topography downstream of non-lithological knickpoints.

alt-text: Fig. 2

~~Fig. 2.~~Fig. 2

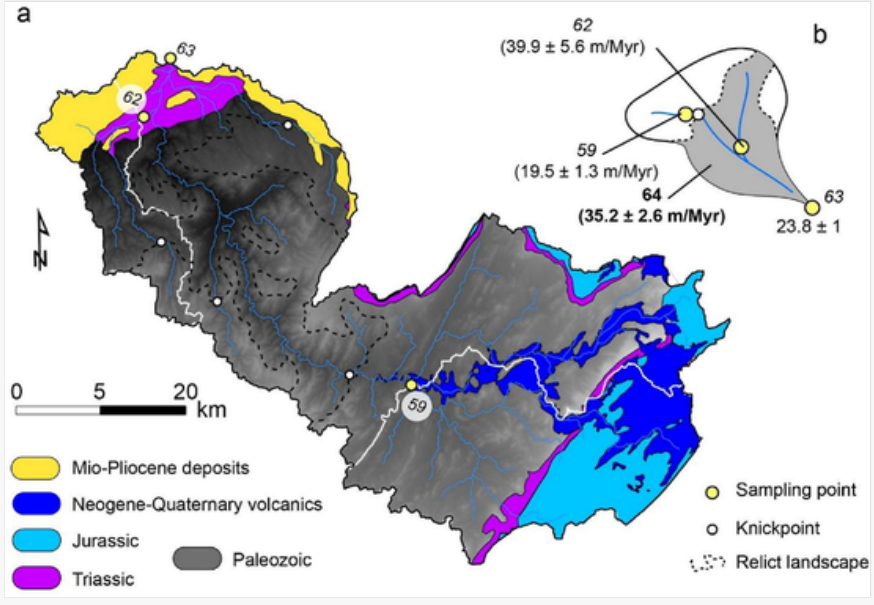

(a) Topographic and geological map of the sampled catchment 63. Note, sampling point 59 is located upstream the non-lithological knickpoint, 62 is downstream the non-lithological knickpoint and 63 represents the mixed rate of basin-wide denudation. (b) Schematic illustration of the catchment 63, showing the correction method to estimate the denudation rate of the downstream portion (64) of the catchment 63, by using drainage area and denudation rate of the basin 63 and 59, respectively. Note, basin-wide denudation derived from basin 62 is consistent with estimate value of the basin 64, both located in the downstream of non-lithological knickpoints.

~~3.3.~~3.3 Predicted ^{10}Be-derived denudations and incision of volcanic bedrock

The basin-averaged k_{sn} values, precipitation rates (IMERG data; Huffman et al., 2015), slope and local relief for the portions of the sampled catchments that include only quartz-bearing lithologies were extracted for comparing ^{10}Be-derived denudation rates. The comparison between denudation rates and k_{sn} allowed extracting the averaged erodibility parameter K for basement rocks in the Western Meseta and constraining n equal to 1. We also evaluate the power best-fit to better explore the relationship between channel steepness and erosion, and evaluate the power-law coefficients, K and n. Finally, values of k_{sn} values were directly converted to denudation rates (see details in Adams et al., 2020, and Clementucci et al., 2022).

To compare our inferred and measured, short-term denudation rates, with longer-term rates we estimated fluvial incision rates by using the 1-Myr-old lava flows as a temporal and geometrical benchmark because they were emplaced over the relict and the rejuvenated landscape of the WMM domain (Tephrite and Basanite data from Rachdi, 1995).

~~3.4.~~3.4 Rock uplift history

To unravel the rock uplift rates over time, we performed a linear inversion of the rivers draining the Paleozoic basement in the Moroccan Meseta domain. We constrained the averaged erodibility value (K) of the Paleozoic basement rocks, using the stream power river incision model ($K = E/k_{sn}^n$) for n = 1. The K was estimated using the forced-origin linear regression in the plot k_{sn} and denudation rates. Although the variation of K over time is difficult to constrain, our averaged estimate can be considered reliable because short-term denudation rates are consistent with the long-term exhumation rates derived from thermochronological data over other quiescent sectors of the Atlas-Meseta system (*e.g.*, Anti-Atlas and Haouz basin; Lanari et al., 2020a; Clementucci et al., 2022; Western Meseta; Barbero et al., 2011). Assuming block uplift conditions in a selected catchment (no spatial uplift variations) and n = 1, the travel time of a perturbation along a river profile (τ) is given by:

$$\tau = \int_{xb}^{x} \frac{dx'}{K\, A_0^m\, A(x')^m} \quad (2)$$

By removing K from Eq. (1) we obtain χ. Following the approach of Goren et al. (2014), a non-dimensional uplift can be inferred from the integration of the stream-power model by assuming that trunks with same χ share a common uplift history and organizing the equation in a matrix form for each data point:

$$A^* U^* = z \quad (3)$$

where A^* is an $N\,x\,q$ matrix, q is the number of χ intervals, U^* is the non-dimensional uplift and z is elevation. This is an overdetermined inverse problem, as there are more known data points than unknown parameters. As such, a least-squares estimate for U^* is used (Goren et al., 2014):

$$U^* = U^*_{pri} + \left(A^{*T} A^* + \Gamma^2 I\right)^{-1} {}^{\circ *T} \left(z - A^* U^*_{pri}\right) \quad (4)$$

~~W~~where Γ is a dampening coefficient that determines the smoothness imposed on the solution, I is the $q \times q$ identity matrix and U^*_{pri} represents the prior guess for U^*, estimted by taking the average slope of the χ-plot (Goren et al., 2014)~~.~~ In this way, from the integration of the stream-power model, χ and U^* can be scaled for K to infer rock uplift rates (U) and time (τ):

$$U = KA_0^m U^* \tag{5}$$

$$\tau = \frac{\chi}{KA_0^m} \tag{6}$$

To reduce the noise, we removed streams with a length lower than 10 km. The linear inversion approach is built on the assumption of spatially uniform uplift, which to a first approximation, can be considered reasonable given that the analysed catchments do not cross any fault that may have been active during the late Cenozoic. Moreover, the analysed catchments are entirely in the WWM where they occupy relatively narrow areas, and hence do not record major along-strike variations in uplift rates. Thus, adopting this approach, by combining the inversions from different catchments, it is also possible to investigate spatial variations in rock-uplift histories (Pavano and Gallen, 2021; Racano et al., 2021; Zhong et al., 2022).

Q14

~~4.~~4 Results

~~4.1.~~4.1 Topographic and river analysis

The WMM domain consists of a NE-SW striking, ~~~~130~~ ~~x~~ ×260 km topographic swell, with a maximum elevation of ~1500 m, and a low relief topography that locally has been deeply dissected by fluvial incision (Figs. 3 and 4). Within the WMM, a series of smaller scale geomorphic features such as summit erosional surfaces, ridge crests and fluvial terraces developed onto and inset into the lava deposits are visible (Figs. 4 and 5). The TMA presents a tabular, low-relief topography while the FMA is characterized by an alternation of steep ridges and wide, low-slope valleys (Figs. 3 and S3). Based on the geometry of the river network, the study area was divided into the Central-Western Meseta (CWM), the North-Western Meseta (NWM), and the South-Western Meseta (SWM). The CWM is characterized by rivers draining directly into the Atlantic Ocean, while the rivers of the NWM and SWM represent the main respective tributaries of the Atlantic draining Oued Sebou and Oum Er Rbia (Fig. 3a). A set of regionally widespread non-lithological knickpoints occur at different elevations in the three domains. These features mark a sharp variation in the k_{sn}, local relief and slope between the deep valleys and the upstream landscape (dashed line in Figs. 3a, ~~3~~b and S3). Particularly, high values of k_{sn} (>~~~~80 $m^{0.9}$; Fig. 3b), slope (>~~~~25°; Fig. S3a), and local relief (>~~~~500 m; Fig. S3b), are found in the FMA domain and in the downstream portions of the non-lithological knickpoints of the WMM and the TMA domains. The lowest values of topographic and channel parameters are observed in the lower portions of the landscape (Oum Er Rbia and Sebou basins) and upstream of the non-lithological knickpoints (Figs. 3 and S3).

Images are optimised for fast web viewing. Click on the image to view the original version.

alt-text: Fig. 3

~~Fig. 3.~~Fig. 3

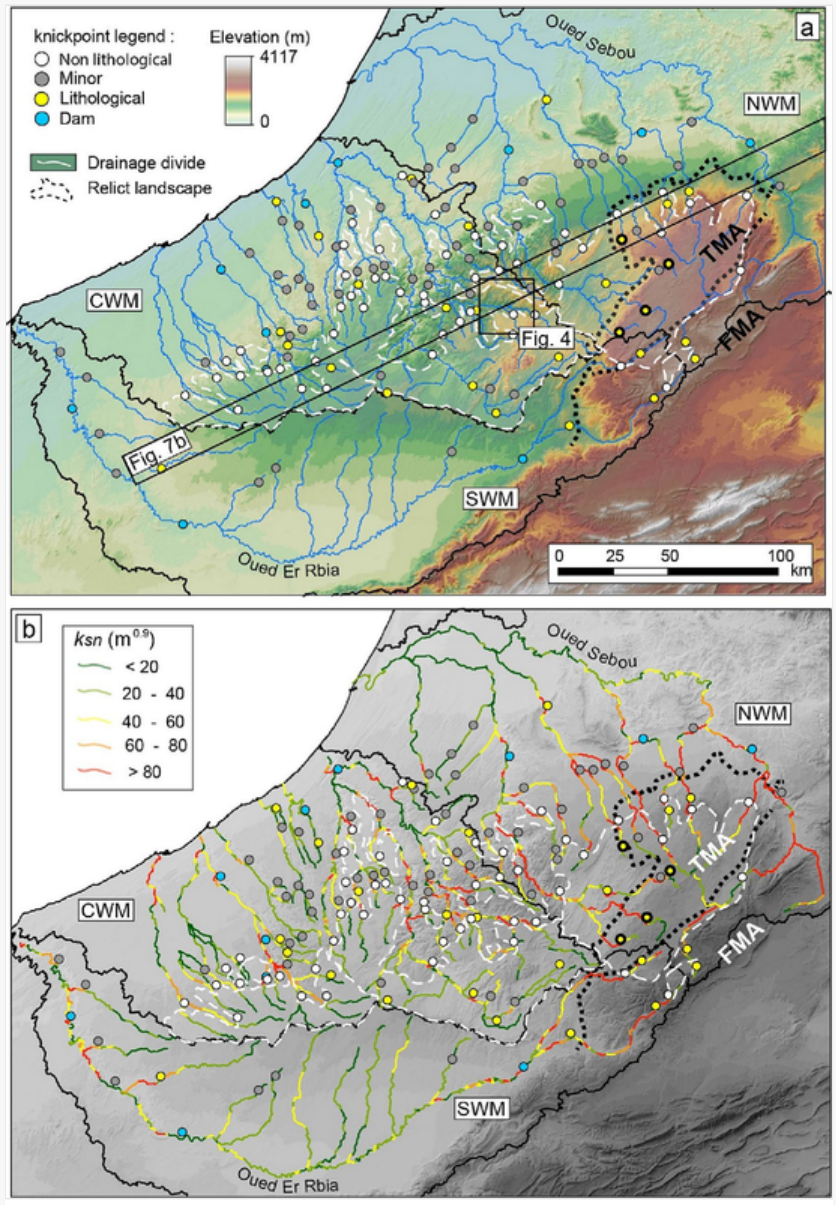

(a) DEM (b) k_{sn} map with main knickpoints. The bold knickpoints demark the escarpment between the TMA and Western Moroccan Meseta (WMM), while the thick dashed line indicates the boundary between the main morpho-structural domains. The solid lines demark the tributaries of the Oued El Rbia (South Western Meseta, SWM), of the Oued Sebou (North Western Meseta, NWM) and rivers draining directly from the Western Meseta to the Atlantic ocean (CWM: Central Western Meseta). TMA and FMA indicate the Tabular Middle Atlas and the Folded Middle Atlas, respectively.

Images are optimised for fast web viewing. Click on the image to view the original version.

alt-text: Fig. 4

~~Fig. 4.~~Fig. 4

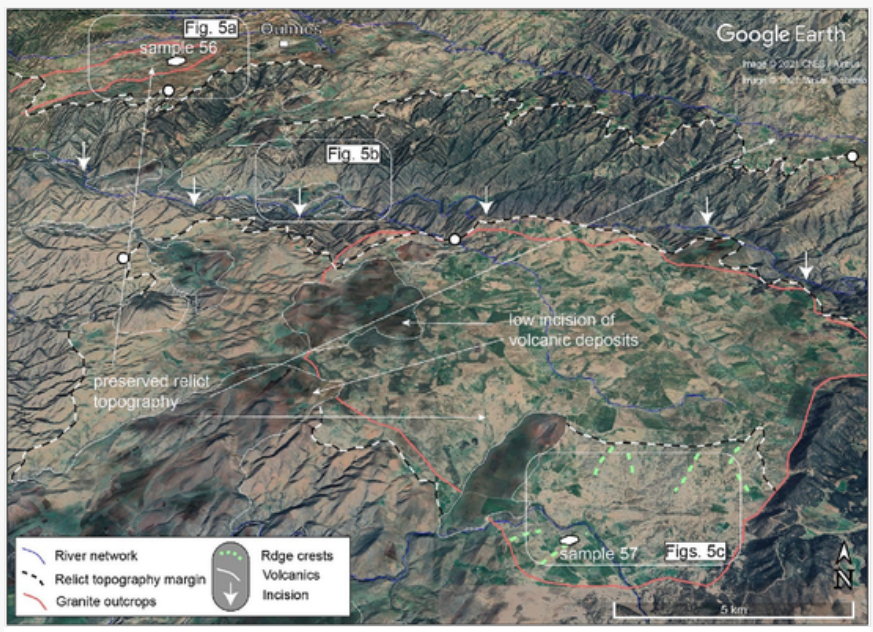

Prospective Google Earth view of the Western Moroccan Meseta. The granite rocks are red polygons and are located at the maximum topography over the summit erosional surface within the sampled catchments 60 and 61 (*i.e.*, relict landscape). The Pleistocene lava flows are deeply incised and well preserved in the deep incisions on the relict topography, respectively. The location of the picture is shown in Fig. 3. (For interpretation of the references to colour in this figure legend, the reader is referred to the web version of this article.)

alt-text: Fig. 5

~~Fig. 5.~~Fig. 5

(a) View of the summit erosional surface of the Western Moroccan Meseta near the locality of Oulmes. The typical morphologies of the granite rocks lying at the maximum elevation are shown in the foreground (black lines). (b) View of the Aguennour River valley. Note the incision across the lava flow deposits (~100 and ~50 m from the top and the base of the lava flow, respectively). (c1-c2) View of the granite outcrops close to the plateau margin. Note the rugged morphologies related to the granite incisions (green lines). The location of the pictures is shown in Fig. 4. (For interpretation of the references to colour in this figure legend, the reader is referred to the web version of this article.)

The NWM sector is characterized by transient longitudinal profiles. Most of the rivers flowing from the TMA and the WMM present lithological knickpoints between 1500 and 2000 m of elevation at χ values of 20 to 25 (Fig. 6a and ~~6~~b). A pattern of widespread non-lithological knickpoints is located between 700 and 1500 m and is associated with a gradual increase in elevation from 200 to 450 km of distance from the river mouth (Fig. 6a and Table S2). These non-lithological knickpoints cluster at χ values of 13 ~~–~~–17 and separate steep downstream segments from low-gradient upstream channels. A cluster of minor knickpoints is located at lower elevations and separates gentle downstream river segments from steeper upstream portions (Fig. 6a and ~~6~~b).

alt-text: Fig. 6

~~Fig. 6.~~Fig. 6

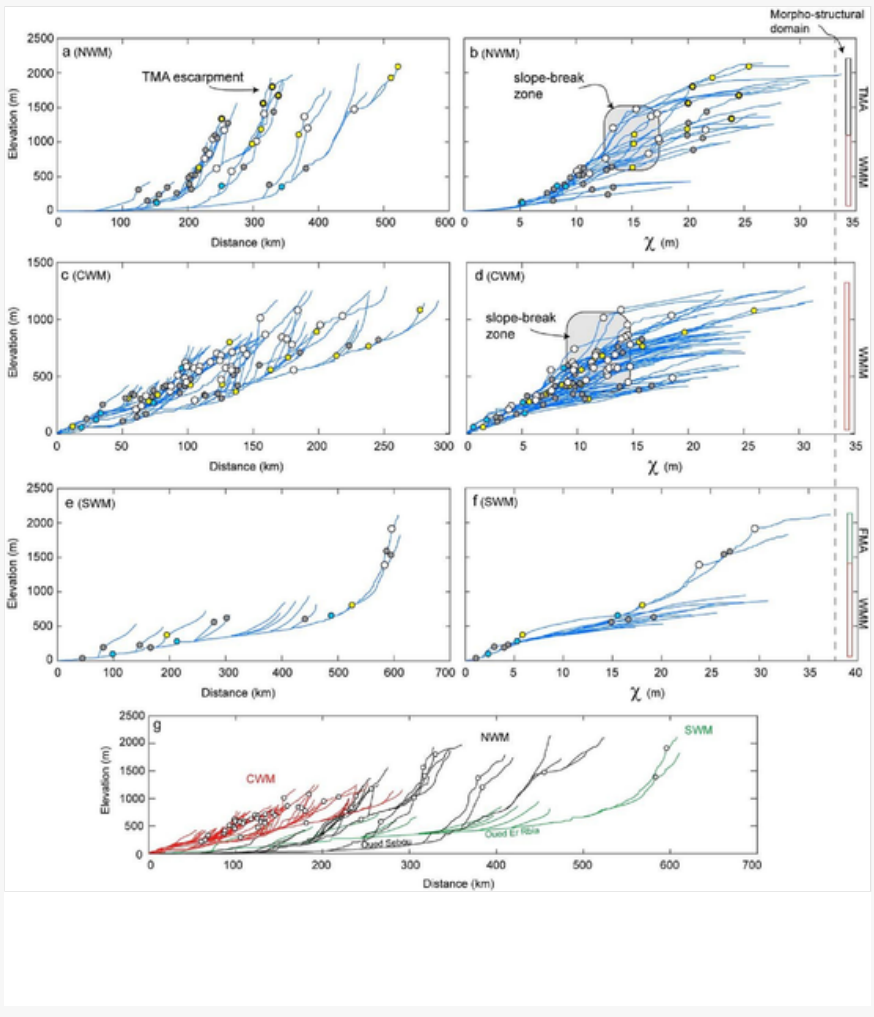

Longitudinal river profiles and χ-z plots with knickpoints for the NWM (a-b), CWM (c-d), and SWM (e-f). The knickpoints legend is in Fig. 2a. The non-lithological knickpoints are located at the slope-break zone separating segments with different k_{sn} value. (g) Longitudinal river profiles with the major non-lithological knickpoints for the three morpho-structural domains. Red rivers: CWM sector; black rivers: NWM sector; green rivers: SWM sector. The non-lithological knickpoints mark the boundary between the downstream steep river profiles and the upstream low-gradient river segments, describing a paleo-surface margin. Note, the rivers of NWM and SWM sectors come mainly from the most elevated TMA and FMA domains, respectively. (For interpretation of the references to colour in this figure legend, the reader is referred to the web version of this article.)

Rivers of the CWM sector show concave-up longitudinal profiles downstream of the non-lithological knickpoints and straight low-gradient upper segments (Fig. 6c). These non-lithological knickpoints present a progressive increase in elevation from 300 m close to the river mouth to ~1000 m upstream toward theTMA domain. Most of these non-lithological knickpoints cluster at χ values of 10~~–~~–15, and separate downstream steep segments from low-gradient upstream portions (Fig. 6d). Downstream of these non-lithological knickpoints, the river segments are characterized by gentle low-gradient river profiles, which contain several minor knickpoints (Fig. 6c).

The SWM sector is characterized by both equilibrated and transient longitudinal profiles. The main slope break is located at high elevation, where two non-lithological knickpoints lie in the FMA domain (~1900 m and ~1500 m; Fig. 6e and ~~6~~f). The average elevations of the non-lithological knickpoints are 627 (σ = 116) m, 1255 (σ = 86) m and 1724 (σ = 135) m for the WMM, TMA and FMA domains, respectively (Table S2).

~~4.2.~~4.2 Long-term river incision

The magnitude of long-term river incision can be estimated by the difference between the reconstructed river profiles projected from the non-lithological knickpoints and the modern base level. Rivers draining the WMM domain (mainly from CWM and NWM sectors) show a mean long-term incision of 415 ($2\sigma = 55$) m, based on 33 river projections (Fig. 7a and Table S3). The mean values of long-term incision of rivers draining the TMA domain is 823 ($2\sigma = 66$) m, based on 8 river projections (Fig. 7a and Table S3). The river projections from the FMA domain show an average long-term incision of 1086 ($2\sigma = 64$) m, although based only on 2 rivers (Fig. 7a and Table S3). There, rivers flow along the SWM sector. Overall, both elevations of the non-lithological knickpoints and magnitude of long-term incision increase progressively from the WMM to the TMA and FMA domains (Fig. 7b).

alt-text: Fig. 7

~~Fig. 7.~~Fig. 7

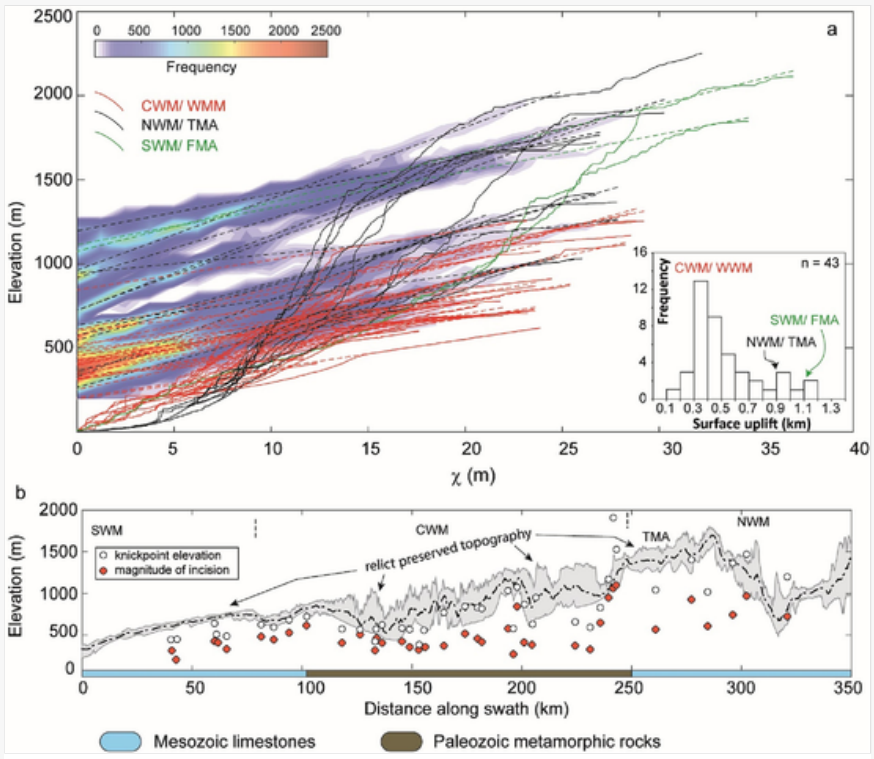

(a) Modern longitudinal profiles and projections of the relict landscape (black dashed segments) upstream of the highest knickpoints using $\theta_{ref} = 0.45$ and the k_{sn} of the relict portion in the χ plot. The main peaks of long-term fluvial incision are at ~400 m and ~800 m in the Western Moroccan Meseta and Tabular Middle Atlas domains, respectively (see details in Table S2). The density distribution legend is relative to the data point of the projected segments. Inset shows the frequency diagrams of the magnitude of long-term incision for the entire dataset (NWM, WMM, SWM). Note, the rivers of NWM and SWM sectors come mostly from the TMA and FMA domains, respectively. (b) Along-strike topographic swath profile, knickpoints elevation and magnitude of long-term incision obtained from the reconstructed river projections. SWM-: South Western Meseta; CWM-: Central Western Meseta; NWM: North Western Meseta; TMA: Tabular Middle Atlas. The location of the swath profile is shown in Fig. 3a.

A few valleys of the WWM have been filled by Quaternary lava flows downstream and upstream of major non-lithological knickpoints (Fig. 1a). Subsequently, these lava flows were dissected through fluvial incision leaving well developed terraces. Downstream of major non-lithological knickpoints, the current valley floor is ~50 and ~100 m below the base and the top of the lava flows, respectively (Figs. 4 and 5b). Considering that the lava yielded radiometric ages of 1 ± 0.1 Ma (Rachdi, 1995), fluvial incision rates vary from ~100 ± 10 to ~50 ± 5 m/Myr, respectively. Importantly, the latter estimate (~50 ± 5 m/Myr) represents the amount of river channel lowering after the lava emplacement using the unconformity as a reference surface (strath of the terrace). Conversely, in the relict surfaces of the WMM domain the lava flows are poorly incised and the fluvial incision rate are <10 m/Myr (Fig. 4).

~~4.3.~~4.3 ^{10}Be-derived denudation rates

^{10}Be concentrations from the largest catchments of the WMM yield denudation rates of 19.8 ± 1.4 and 32.2 ± 2.3 m/Myr (samples 61 and 63; Fig. 1c and Table 1). Denudation rates from the sub-catchments located upstream of the relict landscape are 17.1 ± 1.3 and 19.5 ± 1.4 m/Myr (samples 58 and 59), whereas the sub-catchments downstream of non-lithological knickpoints present rates of 17.4 ± 1.2 and 40.0 ± 5.6 m/Myr (samples 60 and 62; Fig. 1c and Table 1). In the western side of the Moroccan Meseta, sample 53 yields a denudation rate of 14.8 ± 1.0 m/Myr. The unmixed rate from catchment 64 (*i.e.*, the denudation rate of the incised portion of the landscape of catchment 63, which was obtained by subtracting the contribution of the relict landscape of sub-catchment 59 and the area of the steep sub-catchment 62 downstream of non-lithological knickpoints; Fig. 2), yields a denudation rate of 35.2 ± 2.6 m/Myr. This shows a good match with the estimates of denudation from the same sub-catchment 62 (Fig. 2 and Table S1). The sampled catchments are characterized by a uniform distribution of quartz, which is mostly sourced from the lower Paleozoic metamorphic basement, except for samples 60 and 61. These two basins are influenced by the occurrence of two large granite outcrops located in the high-standing low relief surface of the WMM (Fig. 4), which most likely provided more quartz than the Paleozoic metamorphic rocks. Local denudation rates of bare bedrock surfaces on the summit plateau (relict surface) and on the ridge crests of the granite massif vary from 3.5 ± 0.2 to 4.1 ± 0.3 m/Myr (samples 56A, 56B), and from 13.1 ± 0.9 to 14.4 ± 1.0 m/Myr (samples 57A, 57B), respectively (Table 1). It is worth noting that the denudation rates of the granitic ridge crests: 1) are significantly higher than the rates of the flat summit surfaces, and 2) are close to the values determined for the watersheds of samples 60 and 61, where the two granite massifs are exposed and may provide most of the quartz that yielded the measured ^{10}Be concentration.

~~4.4.~~4.4 Basin-wide denudation rates *versus* topographic metrics

The basin-averaged k_{sn} values range from 16.7 to 53.5 $m^{0.9}$ (Fig. 8a and Table S1), while basin-averaged slope values vary from 6 to 13° (Fig. 8b and Table S1) and the basin-averaged local relief range from 222 to 440 m (Fig. 8c and Table S1). The topographic and channel metrics exhibit a medium to low correlation with the basin-wide denudation rates with R^2 of 0.13, 0.61 and 0.71 for k_{sn}, slope and local relief, respectively (dashed lines in Fig. 8a, ~~8~~b, ~~8~~c). However, a stronger correlation between the topographic metrics and basin-wide denudation rates is obtained considering only the catchments characterized by a homogeneous distribution of bearing-quartz lithologies of the Paleozoic basement (*i.e.*, excluding samples 60 and 61, which quartz is mostly sourced from the granites above the elevated flat surfaces). In this case, the coefficient of correlation increases to 0.76, 0.87 and 0.97 for the basin-averaged k_{sn} values, slope, and local relief, respectively (Fig. 8a, ~~8~~b, ~~8~~c). The lowest topographic and channel metrics are observed for samples 53, 58 and 59, which represent the westernmost sample (53) and the samples upstream of the non-lithological knickpoints. Conversely, samples 62 and 64 (downstream of the non-lithological knickpoints) show the highest values of basin-averaged k_{sn} values, slope and local relief, whereas samples 60, 61

and 63, show slightly lower values, because they represent the mixed estimates, giving that both the upstream and downstream portions of the catchments are contributing (Fig. 8a, ~~8~~b, ~~8~~c and Table S1). Finally, basin-wide denudation rates are poorly correlated with the basin-averaged precipitation (R^2 = 0.38; Fig. 8d).

Images are optimised for fast web viewing. Click on the image to view the original version.

alt-text: Fig. 8

~~Fig. 8.~~Fig. 8

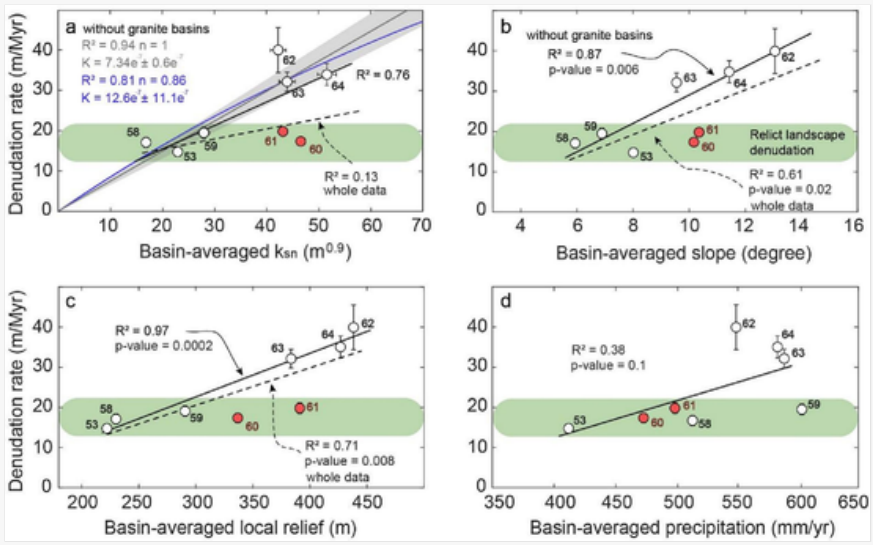

Basin-wide denudation rate *vs* basin-averaged a) k_{sn}, b) slope, c) local relief (2.5 km radius), and d) precipitation rate for the sampled basins. The black and grey solid lines show the bootstrap linear best-fit, and forced linear best-fit without considering basins with exposed granite rocks. The blue trend is the power best-fit. The dashed black lines denote the best-fit considering all sampled basins. The red circles indicate catchments characterized by the contribution of quartz from granite massifs (details in Fig. 4). (For interpretation of the references to colour in this figure legend, the reader is referred to the web version of this article.)

~~4.5.~~4.5 Timing: base-level fall history

To constrain the base level history, the linear inversion of six river profiles has been performed using n = 1, m/n = 0.45 and K of 7.34 ± 0.58 ~~x~~ × 10^{-7} $m^{0.1}$/yr. The parameter n = 1 describes the linear relationship between the erosion rates and k_{sn} (Fig. 8a), as expected for inactive to slow tectonic settings (Godard et al., 2019; Clementucci et al., 2022). The estimation of n has been made testing the stream-power law fits, confirming that the assumption of n = 1 is reasonable (Fig. 8a). The six catchments were selected as they flow over the same rocks from which the K value was estimated (Figs. 9a and S5, S6). Results show similar rock uplift histories (Figs. S5 and S6), which are summarized in Fig. 9b with the mean and the standard error and deviation of the six inversions. Overall, we observe almost constant rock uplift rates of 15-20 m/Myr from 30 to 33 until ~25 Ma, followed by an increase up to ~40 m/Myr between 20 and 15 Ma and by a general decrease to ~25 m/Myr during the last 10 Ma (Fig. 9b). Importantly, within this decreasing trend, a peak in rock-uplift occurs around 5-6 Ma with values of up to 35 m/Myr despite the large standard deviation.

Images are optimised for fast web viewing. Click on the image to view the original version.

alt-text: Fig. 9

~~Fig. 9.~~Fig. 9

Previous Version

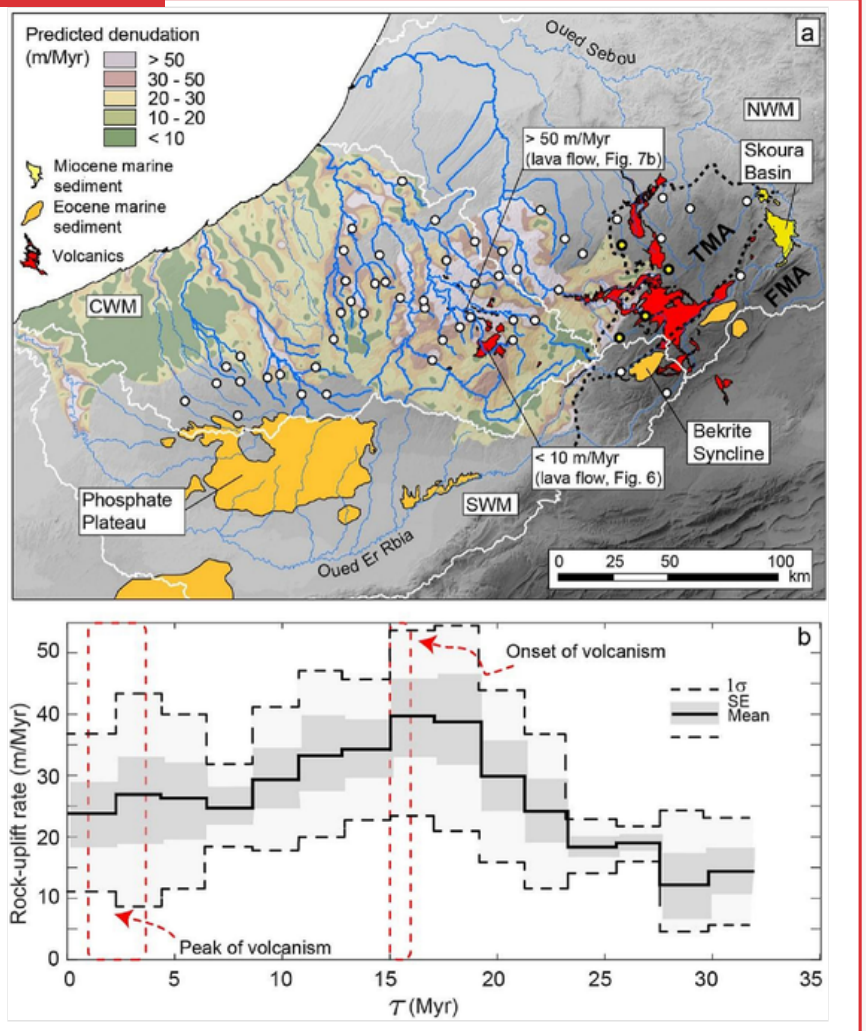

Updated Version

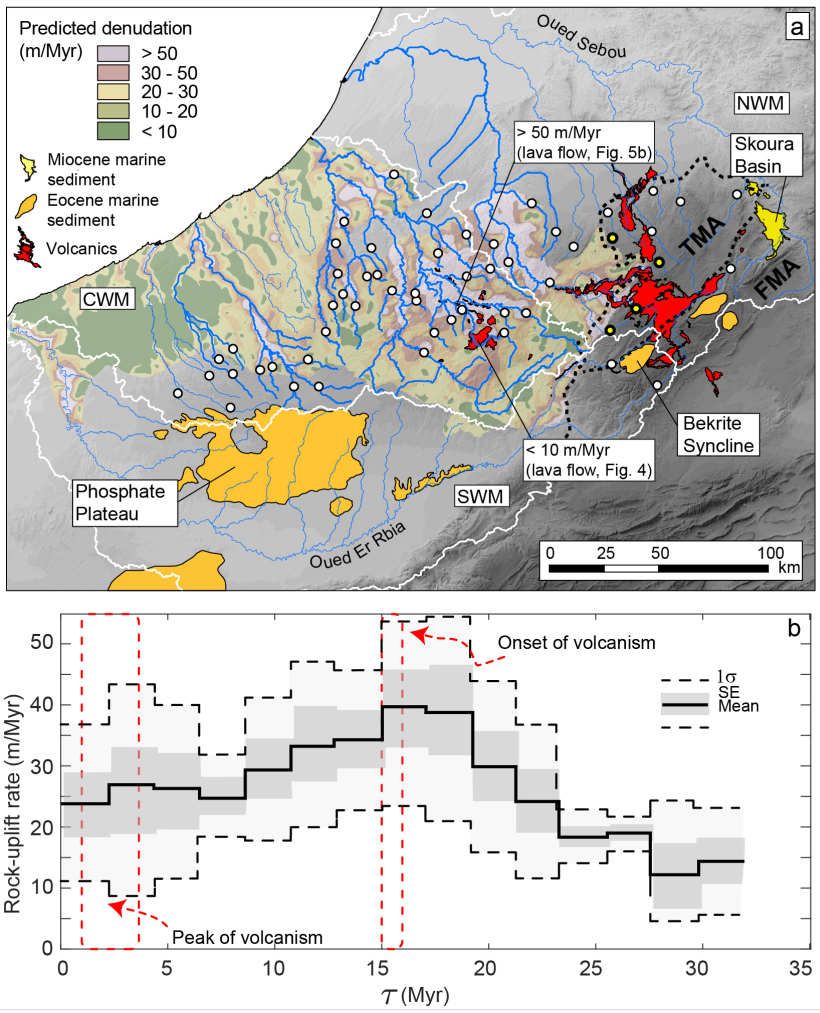

a) Predicted denudation rates based on the distribution of normalized channel steepness in the basement rocks. b) Rock-uplift history for selected rivers (bold blue rivers in Fig. 9a). Mean and standard deviation and error results from the river-profile inversion of six basins of the Western Meseta (details in Figs. S5 and S6 in Supplementary material). (For interpretation of the references to colour in this figure legend, the reader is referred to the web version of this article.)

Replacement Image: T_rU_Meseta_final.jpg

Replacement Instruction: Replace image requested

~~5.~~5 Discussion

~~5.1.~~5.1 Transient topography in Western Moroccan Meseta and Middle Atlas

The study area is characterized by high-standing relict surfaces bounded by non-lithological knickpoints and deeply incised valleys downstream of these knickpoints. This elevated landscape is characterized by low k_{sn} and include low-topographic slopes and local relief surfaces carved onto Paleozoic metamorphic rocks and Mesozoic limestones that gently dip toward the western sectors (Figs. 3, 4, 5; Barbero et al., 2011; ~~Barcos et al., 2014~~(Barcos et al., 2014)). A few lithological knickpoints lie at about 1500 m of elevation at the boundary between the WMM and TMA domains (see bold yellow points in Fig. 6a, ~~6~~b). These knickpoints are marked by a local variation in k_{sn} values and other topographic metrics (slope and local relief) and coincide with a ~500-m-high morphological escarpment representing the stratigraphic contact between the Paleozoic basement and the undeformed Jurassic limestones, reflecting a sharp change in rock erodibility. Conversely, downstream of non-lithological knickpoints the landscape is characterized by steep slopes and k_{sn} values at regional scale (Figs. 3, 4, 5 and S2). This topographic dichotomy suggests that the landscape and hence the river network is not in equilibrium (Crosby and Whipple, 2006; Kirby and Whipple, 2012).

The disequilibrium condition can be explained through several processes, such as drainage reorganization, climate change, eustatic sea-level fall and tectonic uplift (Snyder et al., 2002; Crosby and Whipple, 2006; Kirby and Whipple, 2012; Miller et al., 2013; Boulton et al., 2014; Ballato et al., 2015; ~~Rixhon et al., 2017;~~ (Rixhon et al., 2017); Stokes et al., 2017). In the WMM, a base-level fall due to eustatic forcing is unlikely to be the source of the observed non-lithological knickpoints, because it cannot explain the pattern of k_{sn} values of the river network. Specifically, a wave of knickpoints due to eustatic causes cannot exhibit any major slope break in the chi-space because it is not associated with variations in uplift rate or rock erodibility (Wobus et al., 2006; Kirby and Whipple, 2012; Perron and Royden, 2013). Moreover, there is no geological data documenting a major and protracted sea level drop during the late Cenozoic (Miller et al., 2020) and the glacial-interglacial cycles occurred over the last 1 Ma would result in multiple phases of incision and filling of the coastal area (*e.g.*, Marra et al., 2016), rather than a wave of incision reaching the upper reaches of the Meseta. Drainage reorganization could explain the increase in long-term fluvial incision downstream of the knickpoints due to a gain in drainage area and hence in water discharge (*e.g.*, Yang et al., 2015). However, the non-lithological knickpoints are observed in the watersheds of all domains (WMM, TMA and FMA; Fig. 3), even in small catchments where there is no evidence of drainage reorganization (*e.g.*, wind gaps, knickpoints due to capture processes among others), as instead observed in the Moulouya basin to the east of FMA (~~Bartz et al., 2018~~(Bartz et al., 2018)). Furthermore, increased erosion due to enhanced of average precipitation can also be discarded because it should produce a decrease in the channel slopes downstream of non-lithological knickpoints (Miller et al., 2013; Marder and Gallen, 2023; Figs. 3 and S2). Importantly, the non-lithological knickpoints are characterized by a major upstream decrease in k_{sn} values even across the same lithology as documented in the χ space plots (Fig. 6) and by changes in the topographic slope and local relief at the regional scale (Figs. 3 and S2). This indicates that the knickpoints separate portions of the landscape eroding at different rates (*e.g.*, Crosby and Whipple, 2006; Kirby and Whipple, 2012; Boulton et al., 2014; Olivetti et al., 2016). Consequently, the portion with steep channels downstream of the knickpoints records the response of the fluvial system to an increase in rock uplift rates, while the upstream low relief topography (relict landscape; Fig. 4) records the pre-uplift conditions, as also observed in the others domains of the Atlas-Meseta system (*e.g.*, High Atlas, Siroua and Anti-Atlas range; Boulton et al., 2014; Zondervan et al., 2020; Clementucci et al., 2023). Overall, these observations indicate that the study area experienced a recent topographic rejuvenation (regional, large-scale surface uplift) as documented in other regions worldwide exhibiting similar topographic patterns (Calvet et al., 2015; Miller et al., 2013).

Conversely, minor knickpoints lying at lower elevations can be attributed to Quaternary climate change or a second increase in uplift rates (~~Hancock and Kirwan, 2007~~ (Hancock and Kirwan, 2007); ~~Molnar and England, 1990~~(Molnar and England, 1990)). A similar pattern of minor knickpoints has been described also for the Anti-Atlas domain, where their origin is still enigmatic (Clementucci et al., 2023). In the Western Meseta, these less elevated knickpoints do not present a pronounced break point along the river profiles, but they are evenly distributed along the rivers. Moreover, an increase in rock-uplift is shown around 5-6 Ma in the river-profile inversions. These observations suggest a possible upward knickpoint migration following a second topographic rejuvenation event (*i.e.*, a second increase in uplift rates at 5-6 Ma), which most likely occurred at a larger wavelength from the WMM to the TMA and the FMA (and possibly the HP), as testified by uplifted Messinian marine sediments of the Skoura and Saiss basins (Babault et al., 2008).

~~5.2.~~5.2 Erosional dynamics in the rejuvenated Western Moroccan Meseta

The characterization of a transient landscape is critical for understanding the dynamics of a landscape that includes the coexistence of portions that are in equilibrium with past and present uplift rates. In the Western Meseta the lowest bedrock denudation rates are from granite exposed on the tops of the summit surfaces (3.5 ± 0.2 and 4.1 ± 0.3 m/Myr) while the highest rates are from a similar granite exposed along small ridge crests (13.1 ± 0.9 to 14.4 ± 1.0 m/Myr in Table 1). This four-fold difference is presumably caused by different hillslope processes and higher physical and chemical weathering assuming the same exposure time (Riebe et al., 2004). This demonstrates the key role of hillslope topographic gradients and weathering processes in controlling denudation rates from bedrocks (*e.g.*, Meyer et al., 2010; Godard et al., 2019). In our case, the highest denudation rates occur on the ridge morphologies, at the margin of relict landscape, suggesting an abrupt increase in denudation and hillslope erosion at the transition between the rejuvenated and relict topography, indicating a strong control of the geomorphic domain on the ^{10}Be-derived denudation (Figs. 4 and 5).

Interestingly, the rates of denudation from the ridge crests (samples 57A and 57B) are very similar to those from the watersheds of the same areas (samples 60 and 61). This may be due to the widespread exposure within the catchments of the relict surface sculptured onto the granite rocks that contains a higher amount of quartz than the adjacent metamorphic rocks. These quartz-rich granite rocks erode at relatively low rates (~4 m/Myr) with respect to the basin-wide denudation rates from the catchments composed of metamorphic rocks (>~17 m/Myr) and hence have a higher ^{10}Be concentration than the metamorphic basement. The greater amount of quartz sourced from the relict landscape appears to increase the final ^{10}Be concentration for catchments 60 and 61, producing a decrease in denudation rate estimates. This process is further corroborated by the poor sensitivity of these two watersheds to the linearity between basin-wide denudation rates and topographic metrics that are systematically lower than expected (Fig. 8). Low denudation rates are also observed in watersheds 58 and 59, located upstream of non-lithological knickpoints within the relict portion of the WMM landscape where values of basin-averaged k_{sn}, slope and relief are low. These low denudation rates are consistent with those inferred from the thermochonological data (Barbero et al., 2011) averaged over the last 70 Ma and reflect the erosional decay of topography during a long period of relative base level stability (Calvet et al., 2015). Conversely, watersheds 62 and 63 present higher denudation rates because they receive most of the quartz from the incised landscape downstream of non-lithological knickpoints since the distribution of quartz-bearing rocks is uniform. In this case higher rates reflect the increase in uplift rates as documented in other regions that experienced a topographic rejuvenation (*e.g.*, Olivetti et al., 2016; Miller et al., 2013; Clementucci et al., 2022).

In slow tectonic settings, there is usually a poor correlation between basin-averaged k_{sn} values and denudation rates, and this is generally attributed either to the lithological control on the landscape dynamics or to a decoupling between hillslope and channel incision (*e.g.*, Olivetti et al., 2016; Peifer et al., 2021; Clementucci et al., 2022). Our data show a good correlation between denudation rates and topographic metrics, despite the high degree of transience in the landscape, suggesting that the landscape is not affected by any lithological control and/or decoupling process, except for catchments 60 and 61. In particular, the correlation between basin-wide denudation and k_{sn} suggests that the n parameter of the stream power model can be approximated to 1, as typically observed in slow tectonic settings, where basin-averaged slope and k_{sn} are usually lower than 25° and 200 $m^{0.9}$, respectively (Fig. S4). Finally, the basin-wide denudation rates are insensitive to averaged annual precipitation rates (Fig. 8d),

testifying the lack of a clear dependency of denudation processes to precipitation, as also observed in other slow tectonic ranges characterized by different climatic conditions (Fig. S4; Burbank and Anderson, 2009; Godard et al., 2019; Clementucci et al., 2022).

~~5.3.~~5.3 Topographic evolution and uplift history

The axial zone of the WMM was likely above sea level before the Lutetian (early Cenozoic/middle Eocene) as suggested by the lack of Eocene sediments (Phosphate Plateau), which can be found only along its periphery (Er Rbia Basin) where the phosphatic series shows a deepening and thickening south-westward trend (Fig. 9a; El Kiram et al., 2019). This sedimentation pattern indicates that, while western Morocco was locally subjected to Eocene subsidence and marine sedimentation, the WMM was affected by different processes (Charton et al., 2021). In addition, ~200- to 270-Myr-old apatite fission track cooling ages and associated thermal histories indicate limited vertical movements since the Triassic and suggest that the relict landscape might have started to form even earlier than the Lutetian, possibly from the latest Cretaceous (Barbero et al., 2011; Charton et al., 2021). Our inverted rock uplift rates for the oldest resolved time interval (35–22 Ma) of 10–20 m/Myr are in the same order of magnitude as the ^{10}Be-derived denudation rates averaged over 50 ka (Table 1) and the lava incision rates averaged over the last 1 Ma (see U_1 in Fig. 10a), both for the relict landscape, and the exhumation rates averaged over the last 70 Ma. The occurrence of similar modelled rock uplift and denudation/incision rates across different time scales, could indicate the persistence of a long-term balance between rock uplift and denudation (*i.e.*, steady state denudation; *e.g.*, Whipple, 2001; Willett and Brandon, 2002). However, this observation is based on the overall patterns of denudation at different time scales and does not consider short-term climate fluctuations, which usually precludes the attainment of steady-state conditions over time, possibly triggering rapid changes in denudation rates (Whipple, 2001; Champagnac et al., 2014).

alt-text: Fig. 10

~~Fig. 10.~~Fig. 10

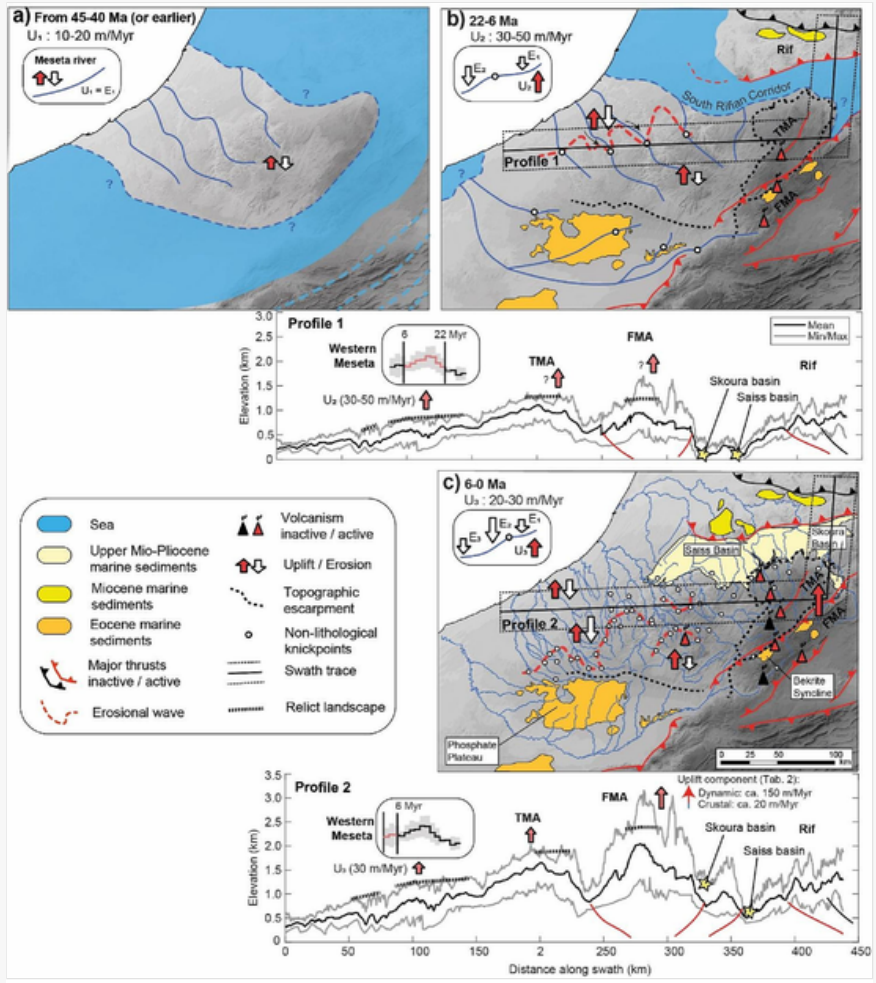

Schematic evolution of the Western Meseta and the Middle Atlas domains since the Lutetian (45–40 Ma). a) Erosional steady-state topography of the Western Meseta with marine conditions in the Middle Atlas and surrounding regions. b) Miocene topographic rejuvenation associated with volcanism and upstream migration of an erosional wave in response to the increase in rock-uplift rates at 22–20 Ma. Note also the southward propagation of the frontal thrusts of the Rif orogenic system with subsidence and marine deposition in the Saiss and the Skoura basins. c) Second slight increase in rock-uplift rates in the Western Meseta. Abrupt increase in uplift rates in the Middle Atlas as testified by uplifted marine Messinian deposits at rates of ~170 m/Myr. Inset in figures b and c show the river profiles and the inverse modelling results of the rivers flowing through the Western Meseta.

Our fluvial inversion results indicate that in the WMM domain, the onset of uplift and associated headward migration of the knickpoints likely started at about 22 Ma and continued until ~10 Ma, with rates ranging from 30 to 50 m/Myr (see U_2 in Fig. 10b). This range of rock uplift rates falls also within the range of ^{10}Be-derived denudation rates and lava flow incision rates downstream of major non-lithological knickpoints (E_2 = 35–55 m/Myr, Figs. 9a and 10b). Barcos et al. (2014) described a maturity stage of the Sebou Basin through a stream length-gradient analysis, which can be a sign of the partial re-equilibrium of these basins since this early Miocene perturbation (Fig. 10b). These portions of the landscape are still eroding at rates that could be representative of the uplift rate U_2 (Fig. 10b). Thus, our inverted rates suggest that the entire WMM started to be uplifted from 22- to 20 Ma, in agreement with the occurrence of uplifted Eocene marine deposits in the WMM and in the axial zone of the FMA and coeval with the onset of Miocene alkaline volcanism (Fig. 10b; Salvan, 1954; El Kiram et al., 2019; El Attmani et al., 2021). Early Miocene uplift initiation could be also coeval with the onset of widespread contractional deformation in the FMA (Gomez et al., 1996, 1998), in the High Atlas Mountains (~~El Harfi et al., 2001~~(El Harfi et al., 2001); Lanari et al., 2020a, 2020b) and in the Rif mountains (Fig. 10b; Abbassi et al., 2020). At the same time, the southward migration of the Rifian frontal thrust produced foreland subsidence with the deposition of unconformable marine deposits in the South Rifian Corridor (Saiss and Skoura Basins; Fig. 10b; Capella et al., 2018). Particularly, the Skoura Basin contains a Messinian shallow-water marine sequence possibly deposited in a gulf bunded by the TMA and FMA (Babault et al., 2008; Capella et al., 2018). In the northern Middle Atlas and the Rif Belt, uplift started sometime after 5–7 Ma (Charriere and Saint-Martin, 1989; Babault et al., 2008) at rates of 170–220 m/Myr as testified by the modern elevation of the Messinian deposits of the Skoura Basin and the closure of the marine South Rifian Corridor (Krijgsman et al., 1999; Babault et al., 2008). This episode of more recent regional uplift was accompanied by a Plio-Quaternary peak in volcanism (Fig. 1) and is also registered by the Western Meseta fluvial network (Fig. 10c). There, our inferred rock uplift rates for the last 5–6 Ma increase up to 35 m/Myr (see U_3 in Fig. 10c). Thus, our modelling rates appear to document a two-stage uplift history of the WMM that includes uplift initiation at 22–20 Ma (with maximum rates reached at about 15 Ma) followed by a second pulse at 5–6 Ma.

Alternatively, the WMM, could have shared an uplift history like that one recorded by the uplifted marine sediment of the Skoura and Saiss Basins (Babault et al., 2008). This implies that the highest knickpoints bounding the elevated relict landscape were originated during the regional 5- to 7-My-old uplift phase (Babault et al., 2008). Although our linear inversion model is calibrated for ^{10}Be data, which integrates erosion rates for the last tens 50.000 years, there are strong indications that short- and long-term, thermochronologically derived, exhumation rates from the relict landscape for the Cenozoic are similar (Barbero et al., 2011). This is also valid for the denudation rates downstream of the most elevated knickpoints, which are consistent with the incision rates inferred from the lava flows over the last 1 Ma. Thus, we can conclude that our inversion is likely not biased by the time scale of the ^{10}Be rates. Moreover, if we apply the approach of profile reconstruction for estimating the timing of the increase in uplift rates, for a surface uplift of 415 +- 55 m (Fig. 7), an erosion rate for the relict landscape up to 20 m/Ma and an uplift (equal to erosion) rate downstream of the knickpoint of 40--50 m/Ma (Fig. 8) we would expect an minimum onset of uplift between 13 and 20 Ma (see equation in fig. 5 of Kirby and Whipple, 2012). These estimates indicate that the uplift rates downstream of the relict landscape are too low to be consistent with a Messinian onset of surface uplift. Thus, the uplift in WMM should have started earlier than 7 Ma. Taken together, these observations suggest that the WMM and the northern sectors of the FMA, where the Skoura Basin is located, did not share the same uplift history pre 7 Ma. Consequently, a two-stage uplift history for the WMM appears to be the most likely scenario.

~~5.4.~~5.4 Implications for uplift mechanisms

The northern sector of Atlas-Meseta system displays a shorter (10--50 km) and longer (>100 km) wavelength topography associated with processes operating at crustal and deeper scale, respectively (Fig. 11; Gomez et al., 1998; Boulton et al., 2014; Miller et al., 2015; Pastor et al., 2015). In particular, the WMM consists of a NE-SW oriented, ~ 130~~-x-~~ x 260 km, ~1500-m-high, topographic swell devoid of Cenozoic deformation (Frizon de Lamotte et al., 2009; Barbero et al., 2011). Barbero et al. (2011) interpreted the WMM as an open, lithospheric-scale fold that formed in response of shortening processes (*i.e.*, lithospheric buckling). Although this mechanism has been documented for specific rheological settings (*e.g.*, Cloetingh and Burov, 2011), there are no geophysical data proving lithospheric folding in the WMM. Alternative mechanisms which could explain the absence of crustal deformation in the WMM and the occurrence of uplift with a topographic wavelength of a several tens of km (up to Q22 ~~more than~~ ≥100 km) is the emplacement of igneous intrusion or magma underplating (*e.g.*, ~~Thybo and Artemieva, 2013~~(Thybo and Artemieva, 2013); Townsend, 2022) and the removal of mantle lithosphere (delamination; *e.g.*, Garzione et al., 2006; Göğüş and Pysklywec, 2008).

Images are optimised for fast web viewing. Click on the image to view the original version.

alt-text: Fig. 11

~~Fig. 11.~~Fig. 11

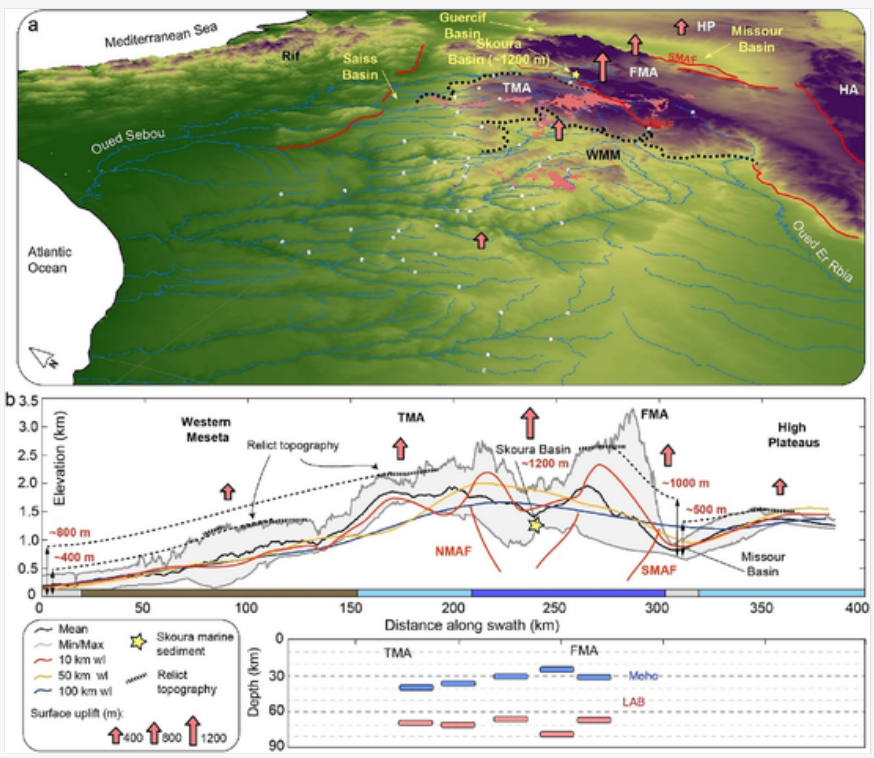

a) Tridimensional view of the northern Atlas-Meseta system. b) Swath profile (details and location are shown in Fig. 1b) with filtered topography at 10--50--100 km wavelengths and data of long-term surface uplift of WMM, TMA, FMA and HP (this work and Pastor et al., 2015). WMM: Western Moroccan Meseta; TMA and FMA: Tabular and Folded Middle Altas; HP: High Plateaus; SMAF: South Middle Atlas Fault; NMAF: North Middle Atlas Fault (after Gomez et al., 1996). The bottom panel indicates the projected position of Moho and lithosphere-asthenosphere boundary (LAB) beneath the Atlas-Meseta system from S-received functions (data from Miller and Becker, 2014).

Following the scenario constrained by our river-profile inversions, the uplift in the WMM started at ~22--20 Ma, shortly before the onset of alkaline volcanism (~16 Ma; El Azzouzi et al., 2010; Fig. 9) and up to 15 Myr earlier than the rise of the northern sectors of the FMA and the South Rifian Corridor (5--7 Ma; Krijgsman et al., 1999; Babault et al., 2008; Fig. 10). These observations suggest that uplift in the WMM would predate the more recent regional uplift and the increase in uplift rates observed at 22--20 Ma must be ascribed to localized processes. The cumulative surface uplift in the WMM is ~415 m with uplift rates varying from 35 to 55 m/Myr during the middle Miocene, and ~30 m/Myr over the last 5--6 Ma (Figs. 9 and 10). These rates indicate that the amount of rock uplift in the last 5--6 Ma would correspond to ~150--180 m. If we consider steady constant denudation of the relict landscape at ~15 m/Myr, the resulting surface uplift during the last 6 Ma will be ~90 m (180---90 m, where 90 m is the surface lowering over the last 6 Ma at 15 m/Myr). Thus, accounting for all the above considerations the cumulative surface uplift pre-6 Ma would be 325 m (415---90 m). Assuming that Airy isostasy is maintained and considering 2.8~~-x-~~ x 10^3 and 3.23~~-x-~~ x 10^3 kg/m^3 as mean crustal (ρc) and asthenospheric mantle (ρa) density respectively, a ~2000-m-thick intrusion will generate ~300 m of surface uplift (note that $(\rho a - \rho c)/\rho c$ is the ratio between elevation gain and crustal thickening; Turcotte and Schubert, 2002). Similarly, if we assume Airy isostasy and a density of the lithospheric mantle (ρm) of 3.3* 10^3 kg/m^3 the same magnitude of surface uplift will be generated by the removal of a ~14-km-thick blob of mantle (note that $(\rho m - \rho a)/\rho a$ is the ratio between elevation gain and thickness of the removed lithospheric mantle; Q23 ~~Molnar and Stock, 2009~~(Molnar and Stock, 2009)). A similar magnitude of surface uplift (~500 m) has been also documented for the HP, although timing, rates and mechanism of uplift are unknown (Fig. 11; Pastor et al., 2015).

In the FMA the topographic growth reflects the combination of deep-seated and crustal shortening and thickening processes, that led to a cumulative surface uplift of about 1200 m as documented by the river projections from the eastern FMA (Fig. 11). Although we do not know the timing of this surface uplift, the same magnitude of uplift occurred in the northern FMA during the last ~5--7 Ma as documented by the uplifted, Messinian marine deposits of the Skoura Basin that are in unconformity over folded Mesozoic limestones (Babault et al., 2008). Thus, it is reasonable to assume that most of the 1200 m of surface uplift in the entire FMA, were gained between 5- and 7 Ma and the present day. Recent surface uplift is also visible in the southern Rifian Corridor (Saiss and Taza-Guercif basins) where marine sediments experienced ~850 m of surface uplift during the last 6--8 Ma (Krijgsman et al., 1999; Babault et al., 2008). Overall, this configuration suggests that the northern FMA is characterized by a complex long-term history of deformation, uplift, and subsidence predating the last pulse of uplift, which produced ~1200 m of elevation gain at rates of ~170--220 m/Myr (Fig. 10). This renewed uplift is almost coeval with the major, second phase of volcanism centred in the Middle Atlas Mountains (Missenard et al., 2006; El Azzouzi et al., 2010) and could reflect large-scale processes coupled with the reactivation of older tectonic structures (Frizon de Lamotte et al., 2009; Babault et al., 2008) and possibly with the injection of large magmatic bodies within the crust.

Specifically, if we assume that shortening produced crustal thickening and surface uplift without surface erosion and/or sediments deposition while Airy isostasy was approximately maintained, thrusting in the FMA would have produced a surface elevation gain of 150 to 730 m over the last 7 Ma at rates of 20 to 100 m/Myr (Garzione et al., 2006; see equations and assumptions in Table 2). The assumption of no erosion (or very limited and hence neglectable erosion) over the last 7 Ma is justified by the

occurrence of the well-preserved, uplifted, marine deposits. This increase in elevation would correspond to a crustal thickening of 0.8 to 4.0 km, and if we assume an initial crustal thickness of 28–32 km, we will expect a ~29- to 36.7-km-thick crust (Table 2). These predictions agree with crustal thickness estimates obtained by Gomez et al. (1999) and Miller and Becker (2014; Fig. 11). Consequently, the remaining 470–1050 m of surface uplift should reflect deep-seated processes (*i.e.*, mantle driven) at uplift rates of 65–150 m/Myr.

alt-text: Table 2

~~Table 2~~ Table 2

The table layout displayed in this section is not how it will appear in the final version. The representation below is solely purposed for providing corrections to the table. To view the actual presentation of the table, please click on the Preview located at the top of the page.

Structural topographic relief and lithospheric thickening of the Folded Middle Atlas based on the equation of Garzione et al. (2006): $dh/dt = (\rho_m-\rho_c)/\rho_c * (UH/W)$, assuming that Airy isostasy is maintained during shortening and for crustal (ρ_c) and asthenospheric mantle (ρ_m) densities of 2.8 and 3.23 kg/m^3, respectively. Shortening produces thickening and surface uplift at a rate of dh/dt (assuming no surface erosion and subsidence with deposition). The parameters H (crustal thickness) and W (orogen width) at 7 Ma and the inferred thickness after 7 Ma of shortening at rates of 0.5 to 1.5 mm/yr are consistent with modern crustal thickness data reported by Miller and Becker (2014).

W[a] min (km)	W[a] max (km)	H[b] min (km)	H[b] max (km)	U[c] min (mm/yr)	U[c] max (mm/yr)	dh/dt[d] min (mm/yr)	dh/dt[d] max (mm/yr)
70	100	28	32	0.5	1.5	0.021	0.105

Since 7 Ma					
Elevation gain, min (km)	Elevation gain, max (km)	Crustal root[e] min (km)	Crustal root[e] max (km)	Mean thickness of crust[f] min (km)	Mean thickness of crust[f] max (km)
0.15	0.73	0.81	3.96	28.96	36.7

Table Footnotes

[a] Width of the deforming Middle Atlas range.

[b] Initial crustal thickness.

[c] Shortening rate (data from Vernant et al., 2010 and Gomez et al., 1999).

[d] Surface uplift rate assuming lithospheric (ρ_c) and mantle (ρ_m) density of 2.8 and 3.23 kg/m^3 (after Garzione et al., 2006).

[e] Expected crustal root of the thickened crust according to Airy isostatic model (Mean gain elevation*ρ_c)/(ρ_c*ρ_m).

[f] Expected crustal thickness of the thickened crust (H + Elevation gain + Crustal root).

These simple calculations indicate two possible end-member scenarios for the topographic growth of the FMA during the last 5–7 Ma: 1) shortening was the main cause of surface uplift (730 m), which occurred at ~100 m/Myr, while dynamic uplift (470 m) took place at ~65 m/Myr; 2) shortening accounted for a smaller fraction of elevation gain (150 m) and led to uplift at ~20 m/Myr, while dynamic uplift (1050 m) took place at ~150 m/Myr (Table 2). In both cases magma addition may have also, at least locally, influenced to the topographic growth of the FMA, although it is not possible to isolate such a contribution. In any case, if we consider that the volcanic lavas younger than 4 Ma crossing major faults are undeformed, and that the marine deposits of the Skoura Basin are only slightly tilted (<10°), the amount of shortening and thickening during the Plio-Quaternary should be marginal (El Azzouzi et al., 2010; Babault et al., 2008). Thus, the dynamic-supported scenario (option 2) seems to be the most reliable possibility (Fig. 10c profile 2) for the topographic growth of the FMA (Babault et al., 2008).

Finally, the spatial pattern of surface and uplift rates over the last 5–7 Ma, document a large-scale topographic bulge (wavelength > 300 km) centred in the FMA (Fig. 11). In this configuration, the WMM appears to represent the western shoulder of a bulge with uplift at rates that are 2.5 to 6 times lower than those inferred from the central bulge (Figs. 10c and 11b). This large wavelength signal can be explained as results of lithospheric delamination/dripping or upwelling of asthenospheric mantle associated with even deeper processes like the rise of plumes possibly sourced from the Canary hotspot, or a combination of both (Duggen et al., 2009; Miller and Becker, 2014; Miller et al., 2015). Although a large number of geophysical studies robustly detected a shallow LAB and Moho beneath the Middle Atlas, the nature of the regional, deep dynamic processes is still under debate (*e.g.*, Missenard et al., 2006; Clementucci et al., 2023). Given the wavelength and the amplitude of the most recent uplift event and the characteristics of coeval volcanism, we tend to favour the plume hypothesis. Dynamic rising of asthenospheric mantle can reconcile the occurrence of large-scale surface uplift, non-isostatically compensated topography, anomalous thinning of the crust and lithospheric mantle and intermittent Mio-pliocene alkaline volcanism.

In essence, we conclude that the regional topographic evolution of the northern Atlas-Meseta system can result from the contribution of deep components (plume activity and mantle lithospheric delamination) coupled with smaller-scale processes such as possible injection of magmatic bodies within the crust and crustal shortening and thickening, at least for the structural domains characterized by contractional deformation (*e.g.*, Middle and High Atlas).

~~6.~~6 Conclusion

Our study allows the ~~characterisation~~characterization of the magnitude, timing, and rates of the long-term topographic evolution of the northern domains of the Atlas-Meseta system. The preserved relict landscape standing at a high elevation and the occurrence of deeply incised valleys downstream of major non-lithological knickpoints document a transience in topography and hence different stages of topographic evolution. Specifically, the ancient relict topography displays low relief, slope, and k_{sn} values in association with low rates of denudation on both bedrock and watersheds (from 4 to 20 m/Myr). Conversely, the downstream portion of the landscape exhibits higher topographic metrics and denudation rates (up to 40 m/Myr) in response to an increase in rock uplift rate that led to a topographic rejuvenation. Within this general trend a few exceptions emerge. In certain catchments of the Western Meseta, the granite massifs exposed on top of the relict landscape provide a higher amount of quartz than the downstream metamorphics, resulting in a mixed signal of ^{10}Be concentration, giving lower denudation rates than expected. These findings highlight that the uneven distribution of quartz-bearing rocks in the sampled catchments and their relative location within the topographic sectors (*i.e.*, relict *vs* rejuvenated landscape) represent a critical point for deriving basin-wide denudation rates.

Combined with geological data, our river-profile inversion results suggest that the elevated relict surfaces of the WMM have been forming since the Eocene. Moreover, our inverted uplift rates indicate that surface uplift and associated knickpoints migrations started at ~22–20 Ma and reached peak values of ~55 m/Myr at ~15 Ma, while the relict portion of the WMM has been eroding steadily at an average of 15 m/Myr. These values agree with our basin-wide denudation and fluvial incision rates derived from 1-Myr-old lava flows for the relict landscape and the catchment area downstream of non-lithological knickpoints. This Miocene uplift (first uplift phase) of the WMM led to a cumulative surface uplift of ~400 m over a extent of ~130 ~~x~~ × 260 km, and is interpreted to reflect crustal-scale processes such as igneous intrusion or magma underplating.

Subsequently, from 5 to 7 Ma, regional uplift occurred as documented by uplifted, Messinian marine deposits of the Skoura and Saiss basins and minor knickpoints over the WMM domain. Surface uplift inferred from the modern elevation of these marine deposits in the northern FMA (Skoura Basin) is ~1200 m, that agree also with estimates from the western FMA obtained from the river projections. The larger scale (wavelength > 200 km) and the higher magnitude of uplift suggest that mantle processes like upwelling of deep asthenospheric mantle (*i.e.*, plume) may have driven the topographic rejuvenation of the entire Atlas-Meseta system including the WMM (second uplift phase). Uplift occurred at rates ranging from of ~30 to ~170 m/Myr from the WMM to the FMA over a pattern describing a bulge centred in the FMA, where the Plio-Quaternary volcanisms is also centred. The WMM represents the western shoulder of this bulge. Finally, minor crustal thickening induced by shortening may have also contributed to the post 7-Ma topographic growth of the FMA. Overall, these results suggest that uplift in the WMM may have occurred in two major steps at 22–20 and 5–6 Ma, while in the FMA, at least in its northern and western sectors, the major uplift pulse occurred during the last 5–7 Ma.

Uncited references

Gallen and Wegmann, 2017

Salvan and Farkhany, 1982

Declaration of competing interest

The authors declare that they have no known competing financial interests or personal relationships that could have appeared to influence the work reported in this paper.

Acknowledgments

This study is part of the PhD thesis of RC at the University of Roma Tre (PhD Cycle XXXIV). It was supported by the PhD School of Roma Tre and grant "Vinci 2020" awarded to RC (Number: C2-1403). PB was supported by the MIUR (Ministry of Education University and Research), Excellence Department Initiative, Art. 1, com. 314-337, Low 232/2016. The ASTER (CEREGE, Aix-en-Provence) AMS national facility, is supported by the INSU/CNRS, the ANR (Projets thématiques d'excellence programme for the Equipements d'Excellence) and the IRD. We thank G. Aumaître, K. Keddadouche and F. Zaidi for their expertise in AMS measurements, A. Yaaqoub, A. Essaifi, N. Youbi, A. Abbassi and R. Braucher for the stimulating discussions. We are indebted to P-H Blard, S. Willett and T. Schildgen for revising this manuscript as a chapter of the PhD Thesis of the first author, to J. Babault, G. Rixhon and anonymous Reviewers for the excellent and detailed revisions, to the Editor M. Stokes for managing the submission of the manuscript. Finally to L. Benedetti, M. Della Seta, P. Molin and O. Bellier for providing valuable comments during the PhD defense of RC.

~~Appendix A.~~Appendix A Supplementary data

Supplementary data to this article can be found online at https://doi.org/10.1016/j.geomorph.2023.108765.

References

The corrections made in this section will be reviewed and approved by a journal production editor. The newly added/removed references and its citations will be reordered and rearranged by the production team.

Abbassi, A., Cipollari, P., Zaghloul, ~~M. N.~~M.N., Cosentino, D., 2020. ~~The Rif Chain (northern Morocco) in the late Tortonian-early Messinian tectonics of the Western Mediterranean orogenic belt: Evidence from the Tanger-Al Manzla wedge-top basin~~The Rif Chain (northern Morocco) in the late Tortonian-early Messinian tectonics of the Western Mediterranean orogenic belt: evidence from the Tanger-Al Manzla wedge-top basin. Tectonics 39 (9). doi:10.1029/2020TC006164.

Abbassi, A., Cipollari, P., Fellin, ~~M. G.~~M.G., Zaghloul, ~~M. N.~~M.N., Guillong, M., El Mourabet, M., Cosentino, D., 2022. The Numidian sand event in the Burdigalian foreland basin system of the Rif, Morocco, in a source-to-sink perspective. ~~GSA Bulletin~~GSA Bull. 134 (~~9-10~~9–10), 2280–2304. doi:10.1130/B36136.1.

Adams, ~~B. A.~~B.A., Whipple, ~~K. X.~~K.X., Forte, ~~A. M.~~A.M., Heimsath, ~~A. M.~~A.M., Hodges, ~~K. V.~~K.V., 2020. Climate controls on erosion in tectonically active landscapes. ~~Sci. adv.~~Sci. Adv. 6 (42), eaaz3166. doi:10.1126/sciadv.aaz3166.

Agharroud, K., Siame, ~~L. L.~~L.L., Ben Moussa, A., Bellier, O., Guillou, V., Fleury, J., El Kharim, Y., 2021. Seismo-tectonic model for the southern Pre-Rif border (Northern Morocco): insights from morphochronology. Tectonics 40 (4), e2020TC006633. doi:10.1029/2020TC006633.

Arboleya, ~~M. L.~~M.L., Teixell, A., Charroud, M., Julivert, M., 2004. A structural transect through the High and Middle Atlas of Morocco. ~~J. Afr. Earth. Sci.~~J. Afr. Earth Sci. 39 (~~3-5~~3–5), 319–327. doi:10.1016/j.jafrearsci.2004.07.036.

Babault, J., Teixell, A., Arboleya, ~~M. L.~~M.L., Charroud, M., 2008. A Late Cenozoic age for long-wavelength surface uplift of the Atlas Mountains of Morocco. ~~Terra nova.~~Terra Nova 20 (2), 102–107. doi:10.1111/j.1365-3121.2008.00794.x.

Babault, J., Van Den Driessche, J., Charco, M., 2022. 2.10 - plateau uplift, regional warping, and subsidence. In: Shroder, ~~J. F.~~J.F. (Ed.), Treatise on Geomorphology, ~~Second Edition~~Second edition Academic Press, Oxford, pp. 223–269. doi:10.1016/B978-0-12-818234-5.00119-X.

Balco, G., Stone, ~~J. O.~~J.O., Lifton, ~~N. A.~~N.A., Dunai, ~~T. J.~~T.J., 2008. A complete and easily accessible means of calculating surface exposure ages or erosion rates from 10Be and 26Al measurements. Quat. Geochronol. 3 (3), 174–195. doi:10.1016/j.quageo.2007.12.001.

Ballato, P., Landgraf, A., Schildgen, ~~T. F.~~T.F., Stockli, ~~D. F.~~D.F., Fox, M., Ghassemi, ~~M. R.~~M.R., Kirby, E., Strecker, ~~M. R.~~M.R., 2015. The growth of a mountain belt forced by base-level fall: tectonics and surface processes during the evolution of the Alborz Mountains, N Iran. Earth Planet. Sci. Lett. 425, 204–218. doi:10.1016/j.epsl.2015.05.051.

Barbero, L., Jabaloy, A., Gómez-Ortiz, D., Pérez-Peña, ~~J. V.~~J.V., Rodríguez-Peces, ~~M. J.~~M.J., Tejero, R., Estupinan, J., Azdimousa, A., Vazquez, M., Asebriy, L., 2011. Evidence for surface uplift of the Atlas Mountains and the surrounding peripheral plateaux: combining apatite fission-track results and geomorphic indicators in the Western Moroccan Meseta (coastal Variscan Paleozoic basement). Tectonophysics 502 (~~1-2~~1–2), 90–104. doi:10.1016/j.tecto.2010.01.005.

Barcos, L., Jabaloy, A., Azdimousa, A., Asebriy, L., Gómez-Ortiz, D., Rodríguez-Peces, M. J., … Pérez-Peña, J. V., 2014. Study of relief changes related to active doming in the eastern Moroccan Rif (Morocco) using geomorphological indices. J. Afr. Earth Sci. 100, 493–509. https://doi.org/10.1016/j.jafrearsci.2014.07.014.

Bartz, M., Rixhon, G., Duval, M., King, G. E., Posada, C. A., Parés, J. M., Brückner, H., 2018. Successful combination of electron spin resonance, luminescence and palaeomagnetic dating methods allows reconstruction of the Pleistocene evolution of the lower Moulouya river (NE Morocco). Quaternary science reviews 185, 153–171. https://doi.org/10.1016/j.quascirev.2017.11.008.

Borchers, B., Marrero, S., Balco, G., Caffee, M., Goehring, B., Lifton, N., Nishiizumi, K., Phillips, F., Schaefer, J., Stone, J., 2016. Geological calibration of spallation production rates in the CRONUS-Earth project. Quat. Geochronol. 31, 188–198. doi:10.1016/j.quageo.2015.01.009.

Boulton, ~~S. J.~~S.J., Stokes, M., Mather, ~~A. E.~~A.E., 2014. Transient fluvial incision as an indicator of active faulting and Plio-Quaternary uplift of the Moroccan High Atlas. Tectonophysics 633, 16–33. doi:10.1016/j.tecto.2014.06.032.

Braucher, R., Merchel, S., Borgomano, J., Bourlès, ~~D. L.~~D.L., 2011. ~~Production of cosmogenic radionuclides at great depth: A multi element approach~~Production of cosmogenic radionuclides at great depth: a multi element approach. Earth Planet. Sci. Lett. 309 (~~1–2~~1–2), 1–9. doi:10.1016/j.epsl.2011.06.036.

Burbank, ~~D. W.~~D.W., Anderson, ~~R. S.~~R.S., 2009. Tectonic Geomorphology. John Wiley & Sons. doi:10.1002/9781444345063.

Calvet, M., Gunnell, Y., Farines, B., 2015. ~~Flat-topped mountain ranges: Their global distribution and value for understanding the evolution of mountain topography~~Flat-topped mountain ranges: their global distribution and value for understanding the evolution of mountain topography. Geomorphology 241, 255–291. doi:10.1016/j.geomorph.2015.04.015.

Capella, W., Barhoun, N., Flecker, R., Hilgen, ~~F. J.~~F.J., Kouwenhoven, T., Matenco, ~~L. C.~~L.C., Sierro, L.C., Tulbure, M.A., Yousfi, M.Z., Krijgsman, W., 2018. Palaeogeographic evolution of the late Miocene Rifian Corridor (Morocco): reconstructions from surface and subsurface data. ~~Earth-Science Reviews~~Earth Sci. Rev. 180, 37–59.

Carretier, S., Regard, V., Vassallo, R., Martinod, J., Christophoul, F., Gayer, E., Audin, L., Lagane, C., 2015. ~~A note on 10Be-derived mean erosion rates in catchments with heterogeneous lithology: Examples from the western Central Andes~~A note on 10Be-derived mean erosion rates in catchments with heterogeneous lithology: examples from the western Central Andes. ~~Earth Surf. Processes Landforms.~~Earth Surf. Process. Landf. 40 (13), 1719–1729. doi:10.1002/esp.3748.

Champagnac, ~~J. D.~~J.D., Valla, ~~P. G.~~P.G., Herman, F., 2014. Late-Cenozoic relief evolution under evolving climate: a review. Tectonophysics 614, 44–65. doi:10.1016/j.tecto.2013.11.037.

Charriere, A., 1984. Évolution néogène de bassins continentaux et marins dans le Moyen Atlas central (Maroc). Bull. Soc. Géol. Fr. 7 (6), 1127–1136.

Charriere, A., Saint-Martin, J.P., 1989. ~~Relations entre les formations re´cifales du Miocene superieur et la dynamique d'ouverture et de fermeture des communications marines a la bordure me´ridionale du sillon sud-rifain (Maroc)~~Relations entre les formations re'cifales du Miocene superieur et la dynamique d'ouverture et de fermeture des communications marines a la bordure me'ridionale du sillon sud-rifain (Maroc). C. R. Acad. Sci. II 309, 611–614.

Charton, R., Bertotti, G., Arnould, ~~A. D.~~A.D., Storms, ~~J. E.~~J.E., Redfern, J., 2021. ~~Low-temperature thermochronology as a control on vertical movements for semi-quantitative source-to-sink analysis: A case study for the Permian to Neogene of Morocco and surroundings~~Low-temperature thermochronology as a control on vertical movements for semi-quantitative source-to-sink analysis: a case study for the Permian to Neogene of Morocco and surroundings. ~~Basin Research~~Basin Res. 33 (2), 1337–1383. doi:10.1111/bre.12517.

Chmeleff, J., von Blanckenburg, F., Kossert, K., Jakob, D., 2010. Determination of the 10Be half-life by multicollector ICP-MS and liquid scintillation counting. Nucl. Instrum. Methods Phys. Res., Sect. B, Beam Interact. Mater. Atoms. 268 (2), 192–199. doi:10.1016/j.nimb.2009.09.012.

Clementucci, R., 2022. Deciphering mantle contribution on surface uplift in the Atlas-Meseta system (Morocco) (Doctoral dissertation) Earth Sciences. Università degli studi Roma Tre; Aix Marseille Univ. https://tel.archives-ouvertes.fr/tel-03630297/document.

Clementucci, R., Ballato, P., Siame, L., Faccenna, C., Yaaqoub, A., Essaifi, A., Leanni, L., Guillou, V., 2022. Lithological control on topographic relief evolution in a slow tectonic setting (Anti-Atlas, Morocco). Earth Planet. Sci. Lett.. doi:10.1016/j.epsl.2022.117788.

Clementucci, R., Ballato, P., Siame, L., Fox, M., Lanari, R., Sembroni, A., Faccenna, C., Yaaqoub, A., Essaifi, A., 2023. Surface uplift and topographic rejuvenation of a tectonically inactive range: insights from the Anti-Atlas and the Siroua Massif (Morocco). Tectonics 42, e2022TC007383. doi:10.1029/2022TC007383.

Cloetingh, S., Burov, E., 2011. Lithospheric folding and sedimentary basin evolution: a review and analysis of formation mechanisms. Basin Res. 23 (3), 257–290. doi:10.1111/j.1365-2117.2010.00490.x.

Crosby, ~~B. T.~~B.T., Whipple, ~~K. X.~~K.X., 2006. Knickpoint initiation and distribution within fluvial networks: 236 waterfalls in the Waipaoa River, North Island, New Zealand. Geomorphology. 82 (~~1–2~~1–2), 16–38. doi:10.1016/j.geomorph.2005.08.023.

Domènech, M., Teixell, A., Babault, J., Arboleya, M. L., 2015. The inverted Triassic rift of the Marrakech High Atlas: A reappraisal of basin geometries and faulting histories. Tectonophysics 663, 177–191. https://doi.org/10.1016/j.tecto.2015.03.017.

Duggen, S., Hoernle, ~~K. A.~~K.A., Hauff, F., Kluegel, A., Bouabdellah, M., Thirlwall, ~~M. F.~~M.F., 2009. Flow of Canary mantle plume material through a subcontinental lithospheric corridor beneath Africa to the Mediterranean. Geology 37 (3), 283–286. doi:10.1130/G25426A.1.

Dunne, J., Elmore, D., Muzikar, P., 1999. Scaling factors for the rates of production of cosmogenic nuclides for geometric shielding and attenuation at depth on sloped surfaces. Geomorphology 27 (1–2), 3–11. https://doi.org/10.1016/S0169-555X(98)00086-5.

El Attmani, M., Bouwafoud, A., Elouariti, S., Mhamdi, ~~H. S.~~H.S., Bouziane, ~~A. B.~~A.B., Mouflih, M., 2021. The Eocene Bryozoans of Bekrit-Timahdite Formation, Middle-Atlas, Morocco: taxonomy, paleoenvironments and paleoclimates implications. J. Geosci. Environ. Prot. 9 (3), 136–153. doi:10.4236/gep.2021.93008.

El Azzouzi, ~~M. H.~~M.H., Maury, ~~R. C.~~R.C., Bellon, H., Youbi, N., Cotten, J., Kharbouch, F., 2010. Petrology and K-Ar chronology of the Neogene-quaternary Middle Atlas basaltic province, Morocco. Bull. Soc. Géol. Fr. 181 (3), 243–257. doi:10.2113/gssgfbull.181.3.243.

El Harfi, A., Lang, J., Salomon, J., Chellai, E. H., 2001. Cenozoic sedimentary dynamics of the Ouarzazate foreland basin (Central High Atlas Mountains, Morocco). Inter. J. Earth Sci. 90 (2), 393–411. https://doi.org/10.1007/s005310000115.

El Kiram, N., Jaffal, M., Kchikach, A., El Azzab, D., El Ghorfi, M., Khadiri, O., Jourani, E., Manar, A., Nahim, M., 2019. Phosphatic series under Plio-Quaternary cover of Tadla Plain, Morocco: gravity and seismic data. ~~C. R. Geosci.~~Compt. Rendus Geosci. 351 (6), 420–429.

England, P., Molnar, P., 1990. Surface uplift, uplift of rocks, and exhumation of rocks. Geology 18 (12), 1173–1177. doi:10.1130/0091-7613(1990)018<1173:SUUORA>2.3.CO;2.

Faccenna, C., Becker, ~~T. W.~~T.W., 2020. Topographic expressions of mantle dynamics in the Mediterranean. ~~Earth-Science Reviews.~~Earth Sci. Rev. 209, 103327. doi:10.1016/j.earscirev.2020.103327.

Fernandes, ~~V. M.~~V.M., Roberts, ~~G. G.~~G.G., White, N., Whittaker, ~~A. C.~~A.C., 2019. ~~Continental-scale landscape evolution: A history of North American topography~~Continental-scale landscape evolution: a history of North American topography. ~~J. Geophys. Res., Earth Surface~~J. Geophys. Res. Earth Surf. 124 (11), 2689–2722. doi:10.1029/2018JF004979.

Forte, A.M., Whipple, K.X., 2019. Short communication: the Topographic Analysis Kit (TAK) for TopoToolbox. Earth Surf. Dyn. 7, 87–95. doi:10.5194/esurf-7-87-2019.

Frizon de Lamotte, D., Leturmy, P., Missenard, Y., Khomsi, S., Ruiz, G., Saddiqi, O., Guillocheau, F., Michard, A., 2009. Mesozoic and Cenozoic vertical movements in the Atlas system (Algeria, Morocco, Tunisia). An overview. Tectonophysics 475, 9–28. doi:10.1016/j.tecto.2008.10.024.

Gallen, ~~S. F.~~S.F., 2018. Lithologic controls on landscape dynamics and aquatic species evolution in post-orogenic mountains. Earth Planet. Sci. Lett. 493, 150–160. doi:10.1016/j.epsl.2018.04.029.

Gallen, ~~S. F.~~S.F., Wegmann, ~~K. W.~~K.W., 2017. ~~River profile response to normal fault growth and linkage: An example from the Hellenic forearc of south-central Crete, Greece~~River profile response to normal fault growth and linkage: an example from the Hellenic forearc of south-central Crete, Greece. Earth Surf. Dyn. 5 (1), 161–186. doi:10.5194/esurf-5-161-2017.

Garzione, ~~C. N.~~C.N., Molnar, P., Libarkin, ~~J. C.~~J.C., MacFadden, ~~B. J.~~B.J., 2006. ~~Rapid late Miocene rise of the Bolivian Altiplano: Evidence for removal of mantle lithosphere~~Rapid late Miocene rise of the Bolivian Altiplano: evidence for removal of mantle lithosphere. Earth Planet. Sci. Lett. 241 (~~3-4~~3–4), 543–556. doi:10.1016/j.epsl.2005.11.026.

Godard, V., Dosseto, A., Fleury, J., Bellier, O., Siame, L., ASTER Team, 2019. Transient landscape dynamics across the Southeastern Australian Escarpment. Earth Planet. Sci. Lett. 506, 397–406. doi:10.1016/j.epsl.2018.11.017.

Göğüş, ~~O. H.~~O.H., Pysklywec, ~~R. N.~~R.N., 2008. Near-surface diagnostics of dripping or delaminating lithosphere. J. Geophys. Res. Solid Earth 113 (B11). doi:10.1029/2007JB005123.

Gomez, F., Barazangi, M., Bensaid, M., 1996. Active tectonism in the intracontinental Middle Atlas Mountains of Morocco: synchronous crustal shortening and extension. J. Geol. Soc. 153 (3), 389–402. doi:10.1144/gsjgs.153.3.0389.

Gomez, F., Allmendinger, R., Barazangi, M., Er-Raji, A., Dahmani, M., 1998. Crustal shortening and vertical strain partitioning in the Middle Atlas Mountains of Morocco. Tectonics 17 (4), 520–533. doi:10.1029/98TC01439.

Goren, L., Fox, M., Willett, ~~S. D.~~S.D., 2014. Tectonics from fluvial topography using formal linear inversion: theory and applications to the Inyo Mountains, California. J. Geophys. Res. F: Earth Surf. 119 (8), 1651–1681. doi:10.1002/2014JF003079.

Granger, D. E., Kirchner, J. W., Finkel, R., 1996. Spatially averaged long-term erosion rates measured from in situ-produced cosmogenic nuclides in alluvial sediment. The J. Geol. 104 (3), 249–257. http://www.jstor.org/stable/30068190.

Hancock, G., Kirwan, M., 2007. Summit erosion rates deduced from 10Be: Implications for relief production in the central Appalachians. Geology 35 (1), 89–92. https://doi.org/10.1130/G23147A.1.

Hoepffner, C., Soulaimani, A., Piqué, A., 2005. The moroccan hercynides. ~~J. Afr. Earth. Sci.~~J. Afr. Earth Sci. 43 (~~1-3~~1–3), 144–165. doi:10.1016/j.jafrearsci.2005.09.002.

Huffman, ~~G. J.~~G.J., Bolvin, ~~D. T.~~D.T., Braithwaite, D., Hsu, K., Joyce, R., Xie, P., Yoo, ~~S. H.~~S.H., 2015. NASA global precipitation measurement (GPM) integrated multi-satellite retrievals for GPM (IMERG). Algorithm Theoretical Basis Document (ATBD) Version, 4, 26. http://pmm.nasa.gov/sites/default/files/document_files/IMERG_ATBD_V4.5.pdf.

Jolivet, L., Faccenna, C., 2000. Mediterranean extension and the Africa-Eurasia collision. Tectonics 19 (6), 1095–1106. doi:10.1029/2000TC900018.

Kirby, E., Whipple, ~~K. X.~~K.X., 2012. Expression of active tectonics in erosional landscapes. J. Struct. Geol. 44, 54–75. doi:10.1016/j.jsg.2012.07.009.

Korschinek, G., Bergmaierb, A., Faestermanna, T., Gerstmannc, U.C., Kniea, K., Rugela, G., Wallnerd, A., Dillmanna, I., Dollingerb, G., Lierse von Gostomskie, Ch., Kossertf, K., Maitia, M., Poutivtseva, M., Remmer, A., 2010. A new value for the half-life of 10Be by heavy ion elastic recoil detection and liquid scintillation counting. Nucl. Inst. Methods Phys. Res. B. doi:10.1016/j.nimb.2009.09.020.

Krijgsman, W., Langereis, ~~C. G.~~C.G., Zachariasse, ~~W. J.~~W.J., Boccaletti, M., Moratti, G., Gelati, R., Iaccarino, F., Papani, G., Villa, G., 1999. Late Neogene evolution of the Taza–Guercif Basin (Rifian Corridor, Morocc\o) and implications for the Messinian salinity crisis. Mar. Geol. 153 (~~1-4~~1–4), 147–160. doi:10.1016/S0025-3227(98)00084-X.

Lal, D., 1991. Cosmic ray labeling of erosion surfaces: in situ nuclide production rates and erosion models. Earth Planet. Sci. Lett. 104, 424–439. doi:10.1016/0012-821X(91)90220-C.

Lanari, R., Faccenna, C., Natali, C., Şengül Uluocak, E., Fellin, M. G., Becker, T. W., Göğüş, O. H., Youbi, N., Clementucci, R., Conticelli, S., 2023. The Atlas of Morocco: A plume-assisted orogeny. Geochem. Geophys. Geosyst. 24, e2022GC010843. https://doi.org/10.1029/2022GC010843[Instruction: this is goint to be Lanari et al., 2023a].

Lanari, R., Fellin, ~~M. V.~~M.V., Faccenna, C., Balestrieri, ~~M. L.~~M.L., Pazzaglia, ~~F. J.~~F.J., Youbi, N., Maden, C., 2020a. Exhumation and surface evolution of the western high atlas and surrounding regions as constrained by low-temperature thermochronology. Tectonics 39 (3), e2019TC005562. doi:10.1029/2019TC005562.

Lanari, R., Faccenna, C., Fellin, ~~M. G.~~M.G., Essaifi, A., Nahid, A., Medina, F., Youbi, N., 2020b. Tectonic evolution of the western high Atlas of Morocco: oblique convergence, reactivation, and transpression. Tectonics 39 (3), e2019TC005563. doi:10.1029/2019TC005563.

Lanari, R., Reitano, R., Giachetta, E., Pazzaglia, F.J., Clementucci, R., Faccenna, C., Fellin, M.G., 2022. Is the Anti-Atlas of Morocco still uplifting? J. Afr. Earth Sci. 188, 104481. doi:10.1016/j.jafrearsci.2022.104481.

Lanari, R., Boutoux, A., Faccenna, C., Herman, F., Willett, ~~S. D.~~S.D., Ballato, P., 2023. Cenozoic exhumation in the Mediterranean and the Middle East. ~~Earth-Science Reviews~~Earth Sci. Rev. 104328[Instruction: Lanari et al., 2023b].

Marder, E., Gallen, ~~S. F.~~S.F., 2023. Climate control on the relationship between erosion rate and fluvial topography. Geology. doi:10.1130/G50832.1.

Marra, F., Rohling, ~~E. J.~~E.J., Florindo, F., Jicha, B., Nomade, S., Pereira, A., Renne, ~~P. R.~~P.R., 2016. Independent 40Ar/39Ar and 14C age constraints on the last five glacial terminations from the aggradational successions of the Tiber River, Rome (Italy). ~~Earth and Planetary Science Letters~~Earth Planet. Sci. Lett. 449, 105–117. doi:10.1016/j.epsl.2016.05.037.

Meyer, H., Hetzel, R., Fügenschuh, B., Strauss, H., 2010. Determining the growth rate of topographic relief using in situ-produced 10Be: a case study in the Black Forest, Germany. Earth Planet. Sci. Lett. 290 (~~3-4~~3–4), 391–402. doi:10.1016/j.epsl.2009.12.034.

Miller, ~~M. S.~~M.S., Becker, ~~T. W.~~T.W., 2014. Reactivated lithospheric-scale discontinuities localize dynamic uplift of the Moroccan Atlas Mountains. Geology 42 (1), 35–38. doi:10.1130/G34959.1.

Miller, ~~S. R.~~S.R., Sak, ~~P. B.~~P.B., Kirby, E., Bierman, ~~P. R.~~P.R., 2013. ~~Neogene rejuvenation of central Appalachian topography: Evidence for differential rock uplift from stream profiles and erosion rates~~Neogene rejuvenation of central Appalachian topography: evidence for differential rock uplift from stream profiles and erosion rates. Earth Planet. Sci. Lett. 369, 1–12. doi:10.1016/j.epsl.2013.04.007.

Miller, ~~M. S.~~M.S., O'Driscoll, ~~L. J.~~L.J., Butcher, ~~A. J.~~A.J., Thomas, C., 2015. Imaging Canary Island hotspot material beneath the lithosphere of Morocco and southern Spain. Earth Planet. Sci. Lett. 431, 186–194. doi:10.1016/j.epsl.2015.09.026.

Miller, ~~K. G.~~K.G., Browning, ~~J. V.~~J.V., Schmelz, ~~W. J.~~W.J., Kopp, ~~R. E.~~R.E., Mountain, ~~G. S.~~G.S., Wright, ~~J. D.~~J.D., 2020. Cenozoic sea-level and cryospheric evolution from deep-sea geochemical and continental margin records. ~~Science advances~~Sci. Adv. 6 (20), eaaz1346. doi:10.1126/sciadv.aaz1346.

Missenard, Y., Zeyen, H., Frizon de Lamotte, D., Leturmy, P., Petit, C., Sébrier, M., Saddiqi, O., 2006. Crustal versus asthenospheric origin of relief of the Atlas Mountains of Morocco. J. Geophys. Res. Solid Earth 111 (B3). doi:10.1029/2005JB003708.

Molnar, P., England, P., 1990. Late Cenozoic uplift of mountain ranges and global climate change: chicken or egg? Nature 346 (6279), 29–34. doi:10.1038/346029a0.

Molnar, P., Stock, J. M., 2009. Slowing of India's convergence with Eurasia since 20 Ma and its implications for Tibetan mantle dynamics. Tectonics 28 (3). https://doi.org/10.1029/2008TC002271.

Olivetti, V., Godard, V., Bellier, O., ASTER Team, 2016. Cenozoic rejuvenation events of Massif Central topography (France): insights from cosmogenic denudation rates and river profiles. Earth Planet. Sci. Lett. 444, 179–191. doi:10.1016/j.epsl.2016.03.049.

Pastor, A., Babault, J., Owen, ~~L. A.~~L.A., Teixell, A., Arboleya, ~~M. L.~~M.L., 2015. Extracting dynamic topography from river profiles and cosmogenic nuclide geochronology in the Middle Atlas and the High Plateaus of Morocco. Tectonophysics 663, 95–109. doi:10.1016/j.tecto.2015.06.007.

Pavano, F., Gallen, ~~S. F.~~S.F., 2021. A geomorphic examination of the Calabrian forearc translation. Tectonics 40 (7), e2020TC006692. doi:10.1029/2020TC006692.

Peifer, D., Persano, C., Hurst, ~~M. D.~~M.D., Bishop, P., Fabel, D., 2021. Growing topography due to contrasting rock types in a tectonically dead landscape. Earth Surf. Dyn. 9 (2), 167–181. doi:10.5194/esurf-9-167-2021.

Perron, ~~J. T.~~J.T., Royden, L., 2013. An integral approach to bedrock river profile analysis. ~~Earth Surf. Processes Landforms.~~Earth Surf. Process. Landf. 38 (6), 570–576. doi:10.1002/esp.3302.

Racano, S., Schildgen, ~~T. F.~~T.F., Cosentino, D., Miller, ~~S. R.~~S.R., 2021. Temporal and spatial variations in rock uplift from river-profile inversions at the Central Anatolian Plateau southern margin. J. Geophys. Res. F: Earth Surf. 126 (8). doi:10.1029/2020JF006027.

Rachdi, H., 1995. Etude du volcanisme plio-quaternaire du Maroc central: pétrographie, géochimie et minéralogie. Notes Mém. Serv. Géol. Maroc. 381, 157.

Riebe, ~~C. S.~~C.S., Kirchner, ~~J. W.~~J.W., Finkel, ~~R. C.~~R.C., 2004. Erosional and climatic effects on long-term chemical weathering rates in granitic landscapes spanning diverse climate regimes. Earth Planet. Sci. Lett. 224 (~~3-4~~3–4), 547–562. doi:10.1016/j.epsl.2004.05.019.

Rixhon, G., Bartz, M., El Ouahabi, M., Szemkus, N., Brückner, H., 2017. Contrasting terrace systems of the lower Moulouya river as indicator of crustal deformation in NE Morocco. J. Afr. Earth Sci. 126, 45–57. https://doi.org/10.1016/j.jafrearsci.2016.11.005.

Roberts, ~~G. G.~~G.G., White, N., 2010. Estimating uplift rate histories from river profiles using African examples. J. Geophys. Res. Solid Earth 115 (B2). doi:10.1029/2009JB006692.

Rosenkranz, R., Schildgen, T., Wittmann, H., Spiegel, C., 2018. Coupling erosion and topographic development in the rainiest place on Earth: reconstructing the Shillong Plateau uplift history with in-situ cosmogenic ^{10}Be. Earth Planet. Sci. Lett. 483, 39–51. doi:10.1016/j.epsl.2017.11.047.

Salvan, H., Farkhany, M., 1982. Les phosphates de chaux sédimentaires du Maroc. Leurs caractéristiques et leurs problèmes (essai de synthèse). Notes Mem. Serv. Geol. Maroc. 14, 7e20.

Schwanghart, W., Scherler, D., 2014. Short communication: TopoToolbox 2 – MATLAB-based software for topographic analysis and modeling in Earth surface sciences. Earth Surf. Dyn. 2, 1–7. doi:10.5194/esurf-2-1-2014.

Sembroni, A., Kiraly, A., Faccenna, C., Funiciello, F., Becker, ~~T. W.~~T.W., Globig, J., Fernandez, M., 2017. Impact of the lithosphere on dynamic topography: insights from analogue modeling. ~~Geophysical Research Letters~~Geophys. Res. Lett. 44 (6), 2693–2702. doi:10.1002/2017GL072668.

Sembroni, A., Molin, P., Soligo, M., Tuccimei, P., Anzalone, E., Billi, A., Franchini, S., Rinaldi, M., Tarchini, L., 2020. The uplift of the Adriatic flank of the Apennines since the Middle Pleistocene: new insights from the Tronto River basin and the Acquasanta Terme Travertine (central Italy). Geomorphology 352, 106990. doi:10.1016/j.geomorph.2019.106990.

Smith, ~~A. G.~~A.G., Fox, M., Schwanghart, W., Carter, A., 2022. Comparing methods for calculating channel steepness index. ~~Earth-Science Reviews~~Earth Sci. Rev. 227, 103970. doi:10.1016/j.earscirev.2022.103970.

Snyder, ~~N. P.~~N.P., Whipple, ~~K. X.~~K.X., Tucker, ~~G. E.~~G.E., Merritts, ~~D. J.~~D.J., 2000. Landscape response to tectonic forcing: digital elevation model analysis of stream profiles in the Mendocino triple junction region, northern California. ~~Geological Society of America Bulletin~~Geol. Soc. Am. Bull. 112 (8), 1250–1263. doi:10.1130/0016-7606(2000)112<1250:LRTTFD>2.0.CO;2.

Snyder, ~~N. P.~~N.P., Whipple, ~~K. X.~~K.X., Tucker, ~~G. E.~~G.E., Merritts, ~~D. J.~~D.J., 2002. Interactions between onshore bedrock-channel incision and nearshore wave-base erosion forced by eustasy and tectonics. ~~Basin Research.~~Basin Res. 14 (2), 105–127. doi:10.1046/j.1365-2117.2002.00169.x.

Stokes, M., Mather, ~~A. E.~~A.E., Belfoul, M., Faik, F., Bouzid, S., Geach, ~~M. R.~~M.R., Cunha, P.P., Boulton, S.J., Thiel, C., 2017. Controls on dryland mountain landscape development along the NW Saharan desert margin: insights from Quaternary river terrace sequences (Dadès River, south-central High Atlas, Morocco). ~~Quaternary Science Reviews~~Quat. Sci. Rev. 166, 363–379. doi:10.1016/j.quascirev.2017.04.017.

Thybo, H., Artemieva, I. M., 2013. Moho and magmatic underplating in continental lithosphere. Tectonophysics 609, 605–619. https://doi.org/10.1016/j.tecto.2013.05.032.

Townsend, M., 2022. Linking surface deformation to thermal and mechanical magma chamber processes. Earth Planet. Sci. Lett. 577, 117272. doi:10.1016/j.epsl.2021.117272.

Turcotte, ~~D. L.~~D.L., Schubert, G., 2002. Geodynamics. Cambridge University Press.

Vernant, P., Fadil, A., Mourabit, T., Ouazar, D., Koulali, A., Davila, ~~J. M.~~J.M., Garate, J., McClusky, A., Reilinger, R., 2010. Geodetic constraints on active tectonics of the Western Mediterranean: implications for the kinematics and dynamics of the Nubia-Eurasia plate boundary zone. ~~Journal of Geodynamics.~~J. Geodyn. 49 (~~3–4~~3–4), 123–129. doi:10.1016/j.jog.2009.10.007.

Whipple, ~~K. X.~~K.X., 2001. ~~Fluvial landscape response time: How plausible is steady-state denudation?~~Fluvial landscape response time: how plausible is steady-state denudation? ~~American Journal of Science~~Am. J. Sci. 301 (~~4-5~~4–5), 313–325. doi:10.2475/ajs.301.4-5.313.

Willett, ~~S. D.~~S.D., Brandon, ~~M. T.~~M.T., 2002. On steady states in mountain belts. Geology 30 (2), 175–178. doi:10.1130/0091-7613(2002)030<0175:OSSIMB>2.0.CO;2.

Wobus, C., Whipple, ~~K. X.~~K.X., Kirby, E., Snyder, N., Johnson, J., Spyropolou, K., Crosby, B., Sheehan, D., 2006. Tectonics from topography: procedures, promise, and pitfalls. In: Special Papers - Geological Society of America, 398. p. 55. doi:10.1130/2006.2398(04).

Yang, R., Willett, ~~S. D.~~S.D., Goren, L., 2015. In situ low-relief landscape formation as a result of river network disruption. Nature 520 (7548), 526–529. doi:10.1038/nature14354.

Zhong, Y., Willett, ~~S. D.~~S.D., Picotti, V., Xiong, J., Zhang, H., 2022. Spatial and temporal variations of incision rate of the middle Yellow River and its tributaries. J. Geophys. Res. Earth Surf. 127 (1), e2021JF006327. doi:10.1029/2021JF006327.

Zondervan, ~~J. R.~~J.R., Stokes, M., Boulton, ~~S. J.~~S.J., Telfer, ~~M. W.~~M.W., Mather, ~~A. E.~~A.E., 2020. Rock strength and structural controls on fluvial erodibility: implications for drainage divide mobility in a collisional mountain belt. ~~Earth and Planetary Science Letters~~Earth Planet. Sci. Lett. 538, 116221. doi:10.1016/j.epsl.2020.116221.

Stone, J. O., 2000. Air pressure and cosmogenic isotope production. *J. Geophys. Res. Solid Earth. 105*(B10), 23753-23759. https://doi.org/10.1029/2000JB900181

Highlights

- We quantify magnitude, timing and rates of Cenozoic uplift in the Atlas-Meseta.
- Basin-wide and bedrock ^{10}Be denudation rates in the relict landscape are <~20 m/Myr.
- Basin-wide ^{10}Be denudation rates in the adjusted landscape are 30~~-~~–40 m/Myr.
- ~400, 800 and 1200 m of surface uplift for Meseta, TMA and FMA, respectively.
- Two possible phases of uplift in Meseta at 22~~-~~–6 Ma and <~6 Ma.

~~Appendix A.~~Appendix A Supplementary data

Multimedia Component 1

Supplementary material

Queries and Answers

Q1

Query: Your article is being processed as a regular item to be included in a **regular issue**. Please confirm if this is correct or if your article should be published in a special issue using the responses below.

Answer: Yes

Q2

Query: Please review the **given names** (no colouring) **and surnames** (highlighted in teal colouring) to make sure that we have identified them correctly and that they are presented in the desired order. Carefully verify the spelling of all authors' names as well. If changes are needed, please provide the edits in the author section.

Answer: Yes

Q3

Query: The **citation** 'Willet and Brandon, 2002' has been changed to match the author name in the reference list. Please check here and in subsequent occurrences, and correct if necessary.

Answer: Reviewed

Q4

Query: The **citation** 'Barbero et al., 2010' has been changed to match the date in the reference list. Please check here and in subsequent occurrences, and correct if necessary.

Answer: Reviewed

Q5

Query: The **citation** 'Charton et al., 2020' has been changed to match the date in the reference list. Please check here and in subsequent occurrences, and correct if necessary.

Answer: Reviewed

Q6

Query: Citation "Gomez et al., 1999" has not been found in the reference list. Please supply full details for this reference.

Answer: Done

Q7

Query: Citation "Salvan, 1954" has not been found in the reference list. Please supply full details for this reference.

Answer: Done

Q8

Query: Citation "Domenech et al., 2018" has not been found in the reference list. Please supply full details for this reference.

Answer: Done

Q9

Query: The **citation** 'Gallen, 2017' has been changed to match the date in the reference list. Please check here and in subsequent occurrences, and correct if necessary.

Answer: Reviewed

Q10

Query: Citation "Stone (2000)" has not been found in the reference list. Please supply full details for this reference.

Answer: Done

Q11

Query: Citation "Dunne et al., 1999" has not been found in the reference list. Please supply full details for this reference.

Answer: Done

Q12

Query: Citation "Granger et al., 1996" has not been found in the reference list. Please supply full details for this reference.

Answer: Done

Q13

Query: The **citation** 'Rachidi, 1995' has been changed to match the author name in the reference list. Please check here and in subsequent occurrences, and correct if necessary.

Answer: Reviewed

Q14

Query: The **citation** 'Pavano et al., 2021' has been changed to match the author name in the reference list. Please check here and in subsequent occurrences, and correct if necessary.

Answer: Reviewed

Q15

Query: Citation "Barcos et al., 2014" has not been found in the reference list. Please supply full details for this reference.

Answer: Done

Q16

Query: Citation "Rixhon et al., 2017" has not been found in the reference list. Please supply full details for this reference.

Answer: Done

Q17

Query: Citation "Bartz et al., 2018" has not been found in the reference list. Please supply full details for this reference.

Answer: Done

Q18

Query: Citation "Hancock and Kirwan, 2007" has not been found in the reference list. Please supply full details for this reference.

Answer: Done

Q19

Query: Citation "Molnar and England, 1990" has not been found in the reference list. Please supply full details for this reference.

Answer: Done

Q20

Query: The **citation** 'Burbank and Anderson, 2003' has been changed to match the date in the reference list. Please check here and in subsequent occurrences, and correct if necessary.

Answer: Reviewed

Q21

Query: Citation "El Harfi et al., 2001" has not been found in the reference list. Please supply full details for this reference.

Answer: Done

Q22

Query: Citation "Thybo and Artemieva, 2013" has not been found in the reference list. Please supply full details for this reference.

Answer: Done

Q23

Query: Citation "Molnar and Stock, 2009" has not been found in the reference list. Please supply full details for this reference.

Answer: Done

Q24

Query: Note: The **Uncited References** section comprises references that occur in the reference list but are not available in the body of the article text. Please cite each reference in the text or, alternatively, delete it. Any reference not dealt with will be retained in this section.

Answer: Done

Q25

Query: Have we correctly interpreted the following funding source(s) and country names you cited in your article: "PhD School of Roma Tre; Vinci 2020; MIUR".

Answer: Yes

Q26

Query: Supplementary caption was not provided. Please check the suggested data if appropriate, and correct if necessary.

Answer: I think is fine to call it supplementary material